

Generative AI models enable efficient and physically consistent sea-ice simulations

Tobias Sebastian Finn^{1*}, Marc Bocquet¹, Pierre Rampal²,
Charlotte Durand², Flavia Porro³, Alban Farchi⁴,
Alberto Carrassi³

¹CEREA, ENPC, EDF R&D, Institut Polytechnique de Paris,
6-8 avenue Blaise Pascal, Cité Descartes, Champs-sur-Marne,
Marne-la-Vallée, 77455, France.

²Institut des Geosciences de l'Environnement/CNRS, Grenoble, France.

³Dept. of Physics and Astronomy "Augusto Righi",
University of Bologna, Bologna, Italy.

⁴ECMWF, European Centre for Medium-Range Weather Forecast,
Reading, RG2 9AX, United Kingdom.

*Corresponding author(s). E-mail(s): tobias.finn@enpc.fr;
Contributing authors: marc.bocquet@enpc.fr; pierre.rampal@univ-grenoble-alpes.fr;
charlotte.durand1@univ-grenoble-alpes.fr;
flavia.porro2@unibo.it; alban.farchi@enpc.fr; alberto.carrassi@unibo.it;

Abstract

Sea ice is governed by highly complex, scale-invariant, and anisotropic processes that are challenging to represent in Earth system models. While advanced numerical models have improved our understanding of the sea-ice dynamics, their computational costs often limit their application in ensemble forecasting and climate simulations. Here, we introduce GenSIM, the first generative AI-based pan-Arctic model that predicts the evolution of all relevant key properties, including concentration, thickness, and drift, in a 12-hour window with improved accuracy over deterministic predictions and high computational efficiency, while remaining physically consistent. Trained on a long simulation from a state-of-the-art sea-ice–ocean system, GenSIM robustly reproduces statistics as observed in numerical models and observations, exhibiting brittle-like short-term dynamics while also depicting the long-term sea-ice decline. Driven solely by atmospheric forcings, we attribute GenSIM's emergent extrapolation capabilities to patterns that reflect the long-term impact of the ocean: it seemingly has learned an internal

ocean emulator. This ability to infer slowly evolving climate-relevant dynamics from short-term predictions underlines the large potential of generative models to generalise for unseen climates and to encode hidden physics.

Sea ice regularises the Earth system by driving thermohaline circulation and modulating albedo. At the mechanical scale, its complex dynamics arise from the transition of a fluid flow to a fractured, discrete continuum, marked by scale invariance, multi fractality, and anisotropy [1, 2]. These processes are captured in numerical models through rheologies which govern the simulated mechanical response to external forcings coming from the atmosphere and ocean such as winds, currents, and waves [3]. In particular, a new branch of sea-ice models with brittle-class rheologies [4–8] recently introduced a *damage* variable to parametrise the subgrid fracturing of sea ice and to reproduce the spatial and temporal properties of its dynamics across scales as observed from high-resolution satellite observations [6, 9, 10]. Yet, these rheologies, typically implemented with advanced numerical techniques such as Lagrangian finite elements [5], increase computational cost [7, 11], thereby complicating ensemble forecasts and long-term climate projections.

This highlights a long-standing dilemma: sea-ice models that faithfully reproduce the observed dynamics require either advanced rheologies or kilometre-scale resolutions [10], whereas computationally efficient models sacrifice realism. Computational gains are offered by surrogate models that leverage deep neural network, however, they remain limited to predictions of the sea-ice thickness [12] or have narrow applications [13–15]. Crucially, these models suffer from a loss of small-scale information [12, 16], smoothing [17], and reduced physical consistency [18] compared to physics-based numerical models. Moreover, their auto-regressive predictions risk an error accumulation [19] leading to instabilities in long-term simulations [20].

Generative diffusion and flow matching models [21–25] remedy these limitations by learning to produce diverse realisations conditioned on the current states and external forcings. This enables applications from ensemble generation [26, 27], over weather prediction [28] and downscaling [29], to climate applications [30–32]. When applied to sea-ice predictions, these models can refine sea-ice concentration forecasts [33], generate sea-ice states [34], and predict the sea ice on regional scales [35]. Nonetheless, their iterative generation remains unconstrained by physical bounds, and their inherent computational demands hamper adoption to global-scale predictions.

We resolve this dilemma with GenSIM, the first generative AI-based pan-Arctic sea-ice model that predicts all relevant sea-ice states across spatial scales of 10 km–100 km and temporal scales from 12 hours to multi-decadal climate trends. GenSIM simultaneously achieves: (i) a high computational efficiency—being up to $50\times$ faster than the reference sea ice-ocean configuration neXtSIM-OPA [5, 36, 37]—and (ii) an unprecedented level of physical consistency for AI-based sea-ice models, as exemplified through the strict enforcement of non-negativity for the sea-ice thickness. Instantiated as auto-regressive flow matching model, GenSIM employs a scale-aware transformer architecture and exploits physical localisation by domain decomposition for efficient predictions. Trained on 20 years of neXtSIM-OPA output [36] and validated against

numerical models and satellite observations, GenSIM reproduces realistic the large-scale sea-ice evolution over 30 years, including the warming-climate-driven sea-ice decline, the recent hiatus due to internal variability [38], and multifractal brittle-like short-term dynamics. Despite being forced only by the atmosphere, GenSIM implicitly learns ocean-like patterns in its dynamics and thermodynamics—this emergent capability overcomes the conventional requirement for explicit ocean data. Thus, a generative AI model trained for short-term forecasting can robustly perform long-term multi-decadal predictions and implicitly capture multi-scale physical processes, thereby removing a bottleneck in AI-based Earth system modelling.

1 Sea-ice modelling with GenSIM

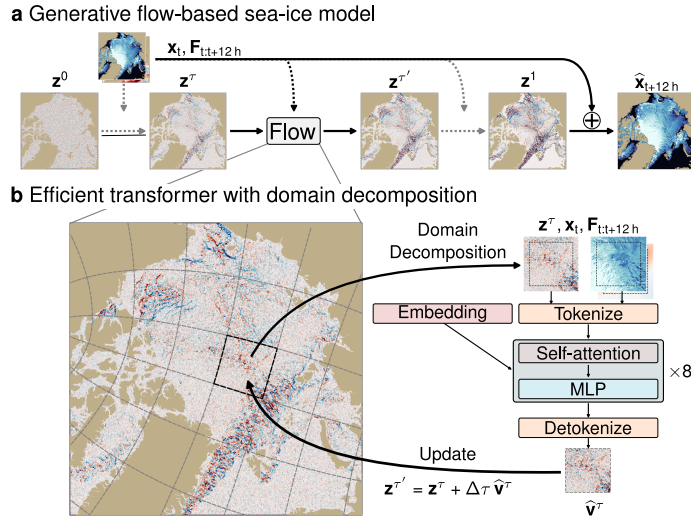


Fig. 1 Schematic of the efficient Arctic-wide generative AI-based sea-ice model GenSIM. Based on flow matching, GenSIM jointly predicts all important sea-ice states for a lead time of 12 hours. (a) Conditioned on initial states \mathbf{x}_t and external atmospheric forcings $\mathbf{F}_{t:t+12\text{h}}$, the model iteratively maps fields of pure noise $\mathbf{z}^0 \sim \mathcal{N}(\mathbf{0}, \mathbf{I})$ to the predicted residual \mathbf{z}^1 , which, added to the initial conditions, results into the prediction $\mathbf{x}_{t+12\text{h}}$ 12 hours later. (b) Within an iterative flow step, here at pseudo time τ , the full Arctic domain is decomposed into overlapping subdomains. A geophysical transformer processes all subdomains in parallel and predicts the velocity of the flow, which is then used to update the state for the next pseudo time τ' . The embedding for modulating the transformer includes information about the pseudo time, data augmentation labels, and used resolution.

GenSIM is a sea-ice model developed to generate 12-hour pan-Arctic forecasts of sea-ice thickness, concentration, damage, velocity components, and snow-on-ice thickness. In addition to the initial conditions, the model accounts for external forcings from the atmosphere: the 2-metre temperature and specific humidity, and 10-metre zonal and meridional wind velocities. To extend the forecast window beyond the trained 12 hours, GenSIM is implemented as an autoregressive system, where each prediction serves as initial condition for the subsequent time step, similar to prediction models

for the atmosphere [28]. Natively operating on a curvilinear $1/4^\circ$ mesh (approximately 12 km resolution), GenSIM makes forecasts in a few seconds and needs below 4 GB memory, which enables forecast ensembles and decadal-long simulations on a single consumer-grade GPU.

Instantiated as flow matching model [24] and conditioned on the initial conditions, \mathbf{x}_t , and forcings, $\mathbf{F}_{t:t+12\text{h}}$, GenSIM produces forecasts by iteratively mapping samples from a Gaussian distribution, \mathbf{z}^0 , to tendency fields, \mathbf{z}^1 , as schematically depicted in Fig. 1a. Adding these tendencies to the initial conditions yields the 12-hour forecast, $\widehat{\mathbf{x}}_{t+12\text{h}}$. Crucially, varying the initial noise sample allows GenSIM to produce diverse forecasts from identical initial conditions and forcings.

Integrated in pseudo time from $\tau = 0$ (pure noise) to $\tau = 1$ (clean tendency), the flow and the underlying dynamical system are defined by its velocity, $\widehat{\mathbf{v}}$. A trained neural network approximates the velocity to propagate the state to the next pseudo-time step, $\mathbf{z}^{\tau'}$, given the intermediate states \mathbf{z}^τ , the initial conditions and forcings, and any relevant embeddings.

Observing the parallels between this generative flow and traditional numerical methods [27], and leveraging the localised physical sensitivity of the tendencies, we introduce a domain decomposition strategy to enhance the computational efficiency at global scale [32, 39]. Instead of processing global fields, the neural network predicts velocities within decomposed subdomains (Fig. 1b). To facilitate the communication between subdomains when integrating the flow, the inputted subdomains overlap, while the velocity prediction itself remains local. This decomposition allows for fully parallel processing and enables linear scaling with the number of global grid points, i.e., the number of subdomains is doubled when the number of global grid points is doubled.

The neural network adopts a scale-aware, mesh-independent transformer architecture, designed to explicitly encode spatial interactions and to accommodate masked land cells. Initially, the network converts the input into tokens through a linear 2×2 patching [40]. These tokens are processed by a series of transformer blocks: self-attention blocks capture spatial dependencies with a learnable localisation that depends on relative distances [41, 42], while light-weighted multi-layer perceptrons (MLPs) non-linearly combine the resulting spatial representations. Derived from the pseudo time and auxiliary labels such as the resolution, a context embedding modulates the input to the attention and MLP layers. After 8 transformer blocks, the tokens are mapped to local velocity predictions via a detokenisation layer.

Sea ice is physically bounded (e.g., the non-negativity of the thickness), and we constrain the generative flow to follow the appropriate bounds [43]. To expose the neural network to bounds during training, we introduce censored flow matching based on variational flow matching [44] and censored Gaussian distributions [34]. The resulting loss function adjusts the usual mean-squared error when encountering bounded data, e.g., over open ocean. There, the loss drives the model towards more extreme values to increase the probability that the bound is exceeded, as concisely exposed in Section 4.3 and detailed derived in Appendix B. This way, the model effectively accounts for the bounds while predicting sea ice.

We trained the model on 20 years (1995–2014) from a long simulation with the coupled sea-ice–ocean neXtSIM-OPA system [36] and forced by the atmosphere with the ERA5 reanalysis [45]. To leverage the scale invariance of sea ice and to enhance mesh and resolution independence, we augmented the data by averaging over randomly drawn kernel sizes up to 8×8 . After averaging, the domain decomposition is implemented during training by randomly slicing subdomains from the pan-Arctic domain to match the subdomain size used during sampling (80×80 grid points, including 8 points overlap in each direction). This efficiently reduced the training cost and enabled us to train the model on fewer GPUs [46]. Finally, we employed distribution augmentation with random flipping and rotations [35, 47] to promote the model’s ability to generalise.

We test GenSIM’s short-term forecasting qualities in a perfect model experiment for 2016–2018, where the simulation of neXtSIM-OPA is our truth, against which we evaluate. Initialised from the simulation and driven by ERA5 forcings, we start a 10-day forecast once a week, effectively performing 153 initialisations. Running an ensemble of 16 members from the same initial conditions and forcings, we compare the performance against persistence forecasts and against a deterministic deep learning model, based on a U-ViT architecture [34] and trained with a mean-squared error loss for the same 12-hour lead time.

Using the root mean-squared error (RMSE) as metric, GenSIM’s ensemble mean outperforms these baselines (Fig. 2a). Across all six predicted variables and all regions, GenSIM improves the scores, reaching an improvement of around 20% compared to the deterministic forecasts. In the central Arctic, which is mostly year-long covered by sea ice, GenSIM achieves substantial improvements, as well as in regions with marginal ice zones (MIZ, Fig. 2b), though small deficiencies in the sea-ice concentration during the change from melting to refreezing remains (see also Fig. A2 and Fig. A3). These results are striking: while the deterministic model is specifically trained to minimise the RMSE, GenSIM—designed as generative flow—achieves an indirect reduction. Derived from independent predictions, GenSIM’s ensemble mean is a true statistical average, explaining why it can outperform the deterministic model [18]. Although well-tuned after 12 hours, GenSIM’s ensemble becomes seemingly underdispersive with increasing lead time, leading to typical spread-skill ratios of 0.8 after 10 days. This underdispersion could be remedied by injecting more stochasticity [28] or tuning on the validation dataset [48] from which we refrain.

Like the geophysical model neXtSIM, GenSIM retains the energy at all scales even after a 10-day forecast (Fig. 2c), while the ensemble mean forecast and the deterministic model lose small-scale energy. This loss of small-scale information effectively smooths the forecast out [12, 35], leading to physical inconsistencies [18] and potentially incurring instabilities in long-term simulations. GenSIM additionally predicts the sea-ice extent more accurately, which becomes especially evident during summer and autumn (Fig. 2d). GenSIM seems to better represent the sea-ice edge and marginal ice zone (MIZ), which we partially attribute to the generative model and partially to the novel censored loss function that explicitly incorporates the physical bounding of variables. These results confirm previous findings for a regional generative sea-ice model [35] and validate that the model works on short time scales. In conclusion,

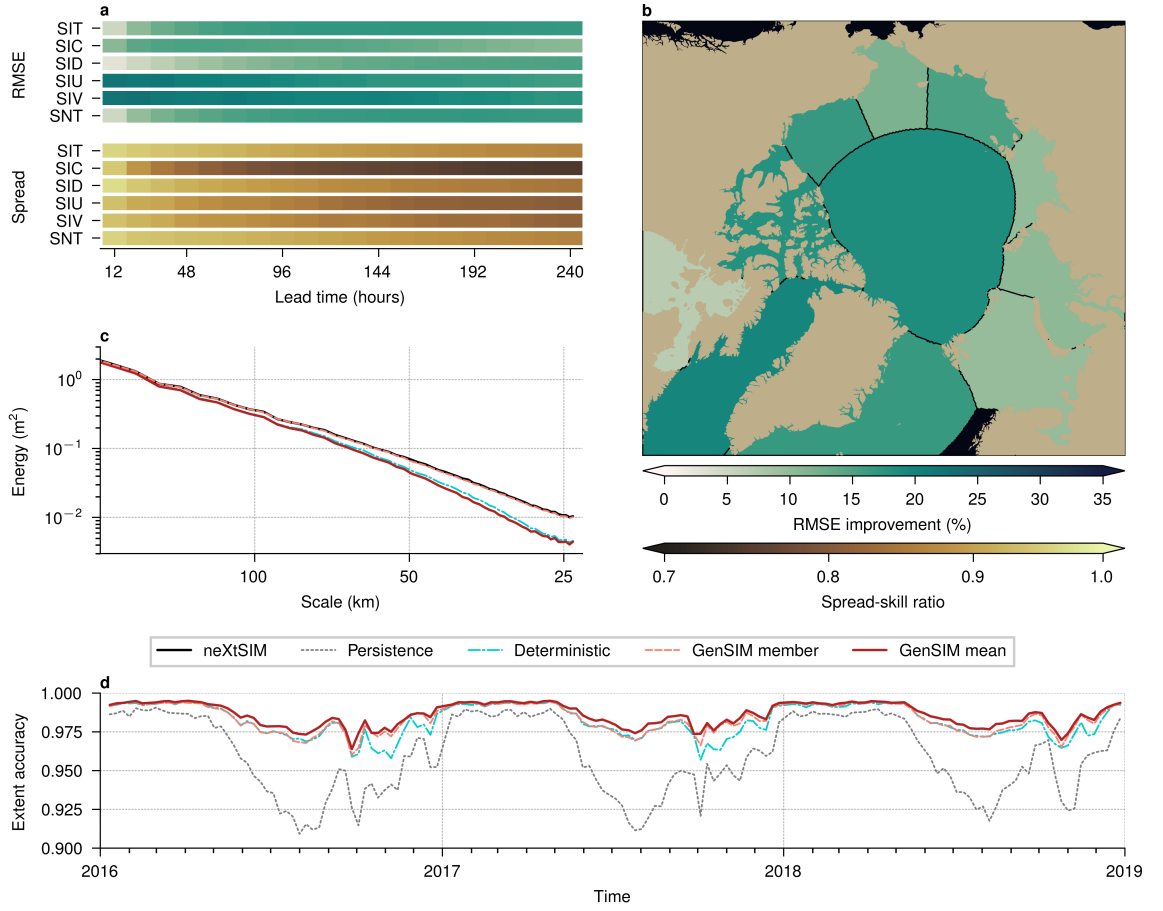


Fig. 2 Overview of GenSIM's short-term forecast qualities. Shown are: (a) the improvement in the root-mean-squared error (RMSE) of GenSIM's ensemble mean compared to the deterministic model and the ratio between the ensemble standard deviation to the RMSE of GenSIM's ensemble mean, both are averaged over all ice-covered grid points (sit=thickness, sic=concentration, sid=damage, siu= u -velocity, siv= v -velocity, snt=snow-on-ice thickness); (b) the 10-day RMSE improvement of GenSIM's ensemble mean to the deterministic model split up into regions, averaged across all six predictive variables after normalizing with their climatology; (c) the 10-day spectrum of the sea-ice thickness in the central Arctic, averaged in log-space across all forecasts; (d) accuracy of the 10-day forecast for the sea-ice extent with the median accuracy for the ensemble members. The used regions for (b) and (c) are depicted in Fig. A1.

GenSIM outperforms the deterministic model and resolves the problems with the loss of small-scale information, like similarly found for the atmosphere [28], while better constraining the MIZ.

2 Realistic long-term simulations through generative short-term predictions

To analyse the long-term behaviour of GenSIM, we perform a long simulation, similar to the neXtSIM-OPA simulation that was used to train our model. Starting with the same initial conditions as neXtSIM-OPA and forced by ERA5, GenSIM is run autoregressively over 1995–2024 with the first five years used as spin-up. Since the model is trained for short-term predictions on data up to 2015, we test GenSIM’s stability over 2000–2014, while we focus on statistical averages and its extrapolation capabilities on the subsequent period. GenSIM’s simulation is benchmarked against the original neXtSIM-OPA simulation and the PIOMAS reanalysis product [49]. For the estimation of the volume, we additionally use a satellite product derived from CryoSat2, and Soil Moisture and Ocean Salinity (SMOS), called CS2/SMOS [50].

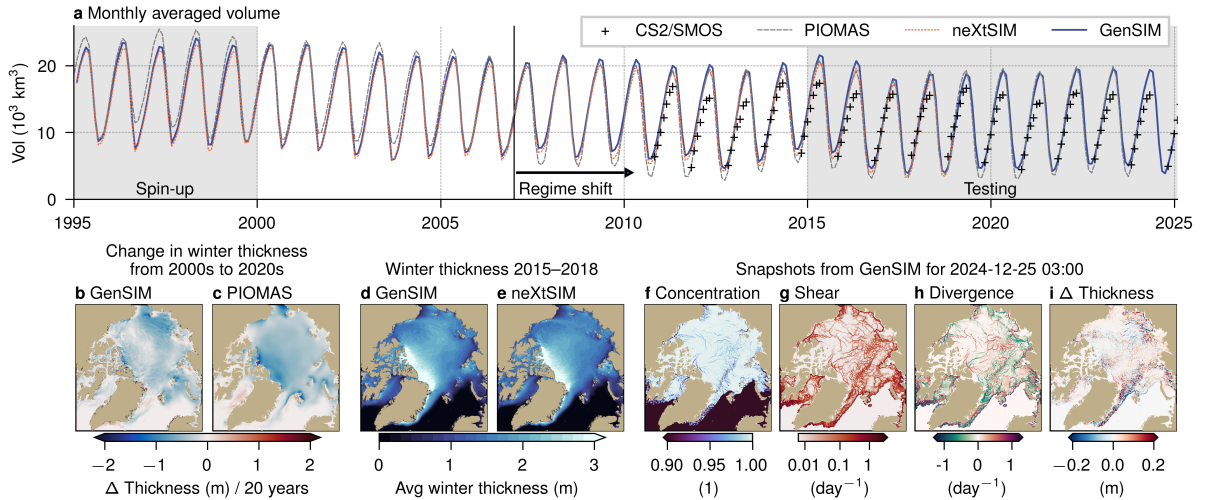


Fig. 3 Overview over GenSIM’s long-term projection qualities. (a) The simulated monthly averaged sea-ice volume (blue line) compared to the simulated volume of neXtSIM (red dotted line) and the retrieved volumes from PIOMAS (grey dashed line) and the merged CryoSAT2-SMOS product (CS2/SMOS, black crosses). (b, c) The change in the winter thickness between 2020–2024 to 2000–2004 for GenSIM and PIOMAS. (d, e) The winter sea-ice thickness averaged between 2015–2018 for GenSIM and neXtSIM. (f–i) Snapshots of GenSIM’s simulation for 2024–12–25 03:00, shown are the sea-ice concentration (f), instantaneous shear rate (g), instantaneous divergence rate (h), and the change in the sea-ice thickness to 2024–12–25 15:00 (i).

GenSIM with its autoregressive steps is remarkably stable over 30 years, even in a warming climate (Fig. 3a): the simulation successfully reproduces observed seasonal cycles and closely aligns with the results from neXtSIM and PIOMAS. Yet, GenSIM is exposed to a small positive bias, especially during summer, attenuating the Arctic sea-ice regime shift post-2007 [51]. As a consequence, GenSIM underestimates the climate change impact for the period 2000–2018 with a linear trend of $224 \text{ km}^3 \text{ year}^{-1}$

compared to $252 \text{ km}^3 \text{ year}^{-1}$ for neXtSIM and $370 \text{ km}^3 \text{ year}^{-1}$ for PIOMAS. Nevertheless, as caused by internal variability, GenSIM successfully exhibits the recent slowing of sea-ice decline consistent with satellite observations and reanalysis datasets [38].

By comparing the spatial distribution of change in average sea-ice thickness between 2000–2004 and 2020–2024 for GenSIM and PIOMAS, the underestimation of the trend becomes especially evident in the central Arctic (Fig. 3b and c). Nevertheless, GenSIM’s sea-ice thickness distribution closely follows neXtSIM’s for 2015–2018 (Fig. 3d and e), even though a small bias towards thicker sea ice persists. The reduced, and in some areas reversed, climate change impact on sea ice surrounding Greenland, potentially attributable to the influx of cooler melt water, is captured by GenSIM. This suggests that GenSIM has learned the well-established relationship between atmospheric near-surface temperature and sea ice from the 2-metre temperature used as external forcing.

The fields generated by GenSIM remain physically consistent, even after 30 years of simulation (Fig. 3f–i). We can track the effect of the short-term dynamics throughout all fields: a reduction in the sea-ice concentration suggests a weakening of sea ice, making it more vulnerable against stress induced by atmospheric winds. The external stress results into a shear and divergent deformation, which are as a diagnostic extracted from the predicted sea-ice velocities. This deformation leads to a redistribution of sea ice with linking divergence to a thinning and convergence to a thickening of sea ice. Although only trained for 12-hour predictions, GenSIM’s largely consistent trend with numerical models and satellite observations, despite a small positive bias, and its physical consistency demonstrates its potential for projecting towards future climate scenarios.

The brittle Bingham-Maxwell rheology [6] employed in neXtSIM is designed to parametrise the short-term subgrid dynamics of sea ice as observed by satellites. The multifractal scaling of GenSIM’s short-term dynamics is analysed based on the sea-ice deformation for the winter in the period 2015–2018, where no high-resolution observations of the sea-ice motion are available.

GenSIM demonstrates its strong skill to reproduce brittle key characteristics of observed Arctic sea-ice deformation from RGPS, while performing comparably to neXtSIM. Although exhibiting more diffuse structures due to its lower resolution (the median resolution of RGPS is around 10 km), GenSIM successfully captures the spatial organisation and intensity of the deformation features from RGPS (Fig. 4a–c) and neXtSIM, including linear kinematic features and high-strain bands.

The scale invariance of sea ice is exposed by the spatial scaling of the distributional moments from the deformation rates with the relation $\langle \dot{\epsilon}_{\text{tot}}^q(L) \rangle \sim L^{-\beta(q)}$ [6, 9]. Here, GenSIM maintains the behaviour of the sea-ice dynamics as modelled by neXtSIM: the heavy-tailed distribution of total deformation rates from GenSIM (Fig. 4d) mirrors neXtSIM’s with a minor underestimation at the highest rates. Moreover, the spatial scaling of GenSIM’s dynamics closely aligns with neXtSIM’s across orders of magnitude (Fig. 4e). The scaling coefficient for the mean ($\beta(q = 1) = 0.13$) is in the range found in other studies [9]. Inferred from the change in the total deformation rate, the

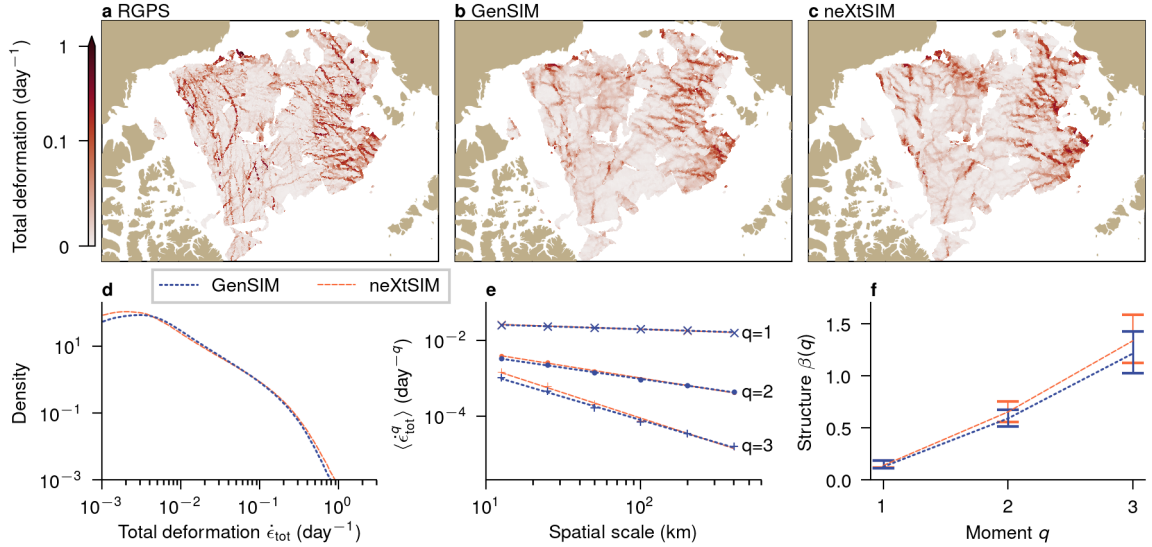


Fig. 4 Fractal scaling of GenSIM’s dynamics. (a–c) Triangulated total deformation rates as inferred from RGPS observations (a), from advecting with GenSIM’s predicted velocities (b), and from advecting with neXtSIM’s predicted velocities (c) for the period 2007-02-01 03:00–2007-02-07 15:00. The deformation rates are estimated at the original data resolution with a nominal time scale of 3 days. (d) Distribution of instantaneous total deformation rates for GenSIM and neXtSIM at the nominal resolution of around 12.5 km. (e) First three distributional moments of the instantaneous total deformation rates with a decreasing coarse-grained resolution. (f) Scaling coefficients of the multifractal structure function $\beta(q)$ from the relation $\langle \dot{\epsilon}_{\text{tot}}^q(L) \rangle \sim L^{-\beta(q)}$ with $L \in [12.5 \text{ km}, 400 \text{ km}]$ for the first three distributional moments q of the instantaneous total deformation rates. The uncertainty in the structure function shows the minimum and maximum in the coefficients estimated based on differences between two successive spatial scales [9, 35]. In (d)–(f), the total deformation rates are estimated based on rectangles defined through the curvilinear mesh in the central Arctic (see also Fig. A1) for January, February, March during the period 2015-01-01 03:00–2018-03-31 15:00.

multifractal structure function, as change of the scaling coefficient with the distributional moment, shows that GenSIM exhibits a similar multifractal scaling to neXtSIM (Fig. 4f).

Trained to predict the sea ice over 12 hours with external atmospheric forcings, GenSIM constrains the short-term dynamics well, producing realistic scale-invariant and anisotropic brittle-like features. However, long-term dynamics and especially the thermodynamics are difficult to learn due to their diminishing signal-to-noise ratio and the missing ocean forcings.

GenSIM is influenced by long-term effects for the thermodynamics and dynamics as similarly found for the coupled neXtSIM-OPA simulation (Fig. 5) with strikingly well matching large-scale patterns. For the thermodynamics, GenSIM exhibits the same zones of ice growth and melting as neXtSIM (Fig. 5, a and b): main growing zones are found in the Laptev sea and Kara sea, as well as the Canadian archipelago and central Arctic, while the most pronounced melting zones are around Greenland, in the Hudson bay, the Barents sea, and the Chukchi sea. In all of these melting zones,

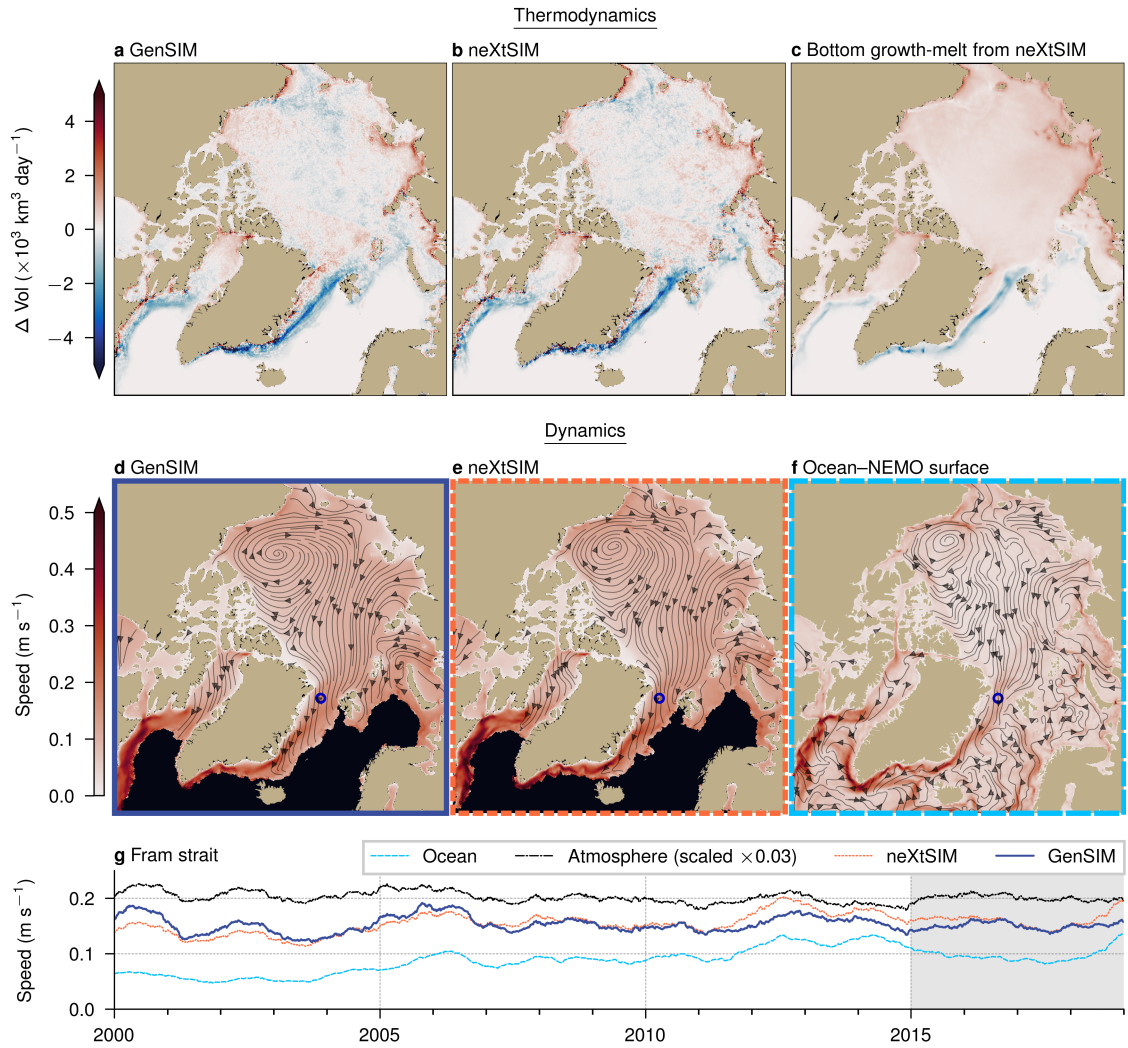


Fig. 5 GenSIM exhibits long-term ocean-like patterns. (a–c) Volume change within 12 hours for (a) GenSIM, (b) neXtSIM, and (c) net bottom growth - bottom melt from neXtSIM, averaged for 2015–2018. The dynamical component caused by advection has been removed from the changes. (d–f) Speed (background) and streamlines (black lines) for (d) sea ice in GenSIM, (e) sea ice in neXtSIM, and (f) ocean surface from the neXtSIM-OPA simulation averaged for 2015–2018; the speed for the dark blue circled position is shown in (g). (g) Time series of speed in the Fram Strait with a year-long averaging filter for long-term tendencies, the shaded area indicates the averaging period for (a–f); note that the atmospheric speed has been scaled down to 3% of its original speed for visualisation purposes.

sea ice is in contact with water coming from the Atlantic or Pacific ocean, connecting them to bottom melting (Fig. 5, c). The neural network correctly identifies these zones such that GenSIM exhibits there similar melting rates as neXtSIM-OPA. Hence, the

learned long-term impact on the growth and melting in GenSIM is similar to the thermodynamical impact from the ocean.

Although the dynamics are dominated by the atmosphere at short time scales [52], they expose a signature from the deeper ocean at longer time scales. Consequently, we find an alignment in the sea-ice drift and the velocity at the ocean surface in coupled sea-ice–ocean simulations (Fig. 5, e and f): sea ice circulates in front of the Alaskan and Canadian coast due to the Beaufort gyre, while the transpolar drift transports sea ice from growing zones to melting zones through the Fram strait. GenSIM’s sea-ice drift matches these major ocean current in the Arctic basin (Fig. 5, d), even though the effective Beaufort gyre is displaced. Moreover, when analysing the sea-ice speed near the Fram strait (Fig. 5, g), GenSIM’s drift has a similar evolution as neXtSIM’s. Notably, GenSIM shows the sea-ice fastening similar to neXtSIM from 2003 to 2008, which remains unexplained by atmospheric forcings but aligns to an increase in the ocean velocity.

GenSIM has seemingly learned the long-term dynamics caused by ocean currents without having access to an external ocean forcing. Combined with the learned long-term thermodynamical patterns, we hypothesise that GenSIM has learned an internal ocean emulator based on the given sea-ice conditions and the external atmospheric forcings. Solely trained by the criterion to predict the tendencies over 12 hours, GenSIM correctly infers slow year-long effects and uncovers hidden dynamics, even when their signal-to-noise ratio is diminishing in the training data. These rather surprising results explain how GenSIM can match its long-term evolution to numerical models and satellite observations in a warming climate.

3 Consequences for AI-based Earth system models

These results pave a way towards the use of generative diffusion and flow matching models for surrogates of other Earth system components than the atmosphere. For sea-ice modelling, they improve upon deterministic models in terms of forecasting scores but also in matching the observed energy spectra at all scales, while being able to produce large forecasting ensembles. These large ensembles are especially useful for sea-ice data assimilation, which has been hindered by high computational costs and the non-existence of adjoints [53]. Hence, generative surrogate models unlock a large potential to improve sea-ice forecasting in the future.

In this study, we built upon the observation that generative flow models work similarly to classical numerical models: they integrate a dynamical system that is defined by the neural network. This similarity allows us to bridge methods used for classical numerical models to surrogate models. Here, we use domain decomposition to efficiently apply such models at global scale. Combined with the employed transformer architecture, the surrogate is flexible in its use with applications from regional to pan-Arctic scales. This flexibility enables us to train generative surrogates across heterogenous datasets and resolutions [32], potentially further boosting their performance.

Our instantiated model, GenSIM, can extrapolate to long-term climate conditions, suggesting that generative surrogates can generalise short-term training objectives

to long-term projections. We partially attribute this stability to GenSIM’s physical consistency: since the effects of the underlying physics are exposed by correlations that change over time, this physical consistency is a strength of generative diffusion and flow matching models, which excel in learning high-dimensional correlations across scales. Furthermore, when each autoregressive prediction time step is initialised from the same noise, GenSIM becomes unstable after the first iteration, indicating the importance of its stochastic generation process. Therefore, the long-term stability is likely an inherently emerging capability of generative flows employed for surrogate modelling.

The successful extrapolation to long-term evolutions from short-term objectives emerges from learning the influence of slow components on the faster, targetted, time scales. This allows us for example to unveil the ocean impact on sea ice, even when GenSIM is solely forced by the atmosphere. Consequently, generative flow models can uncover hidden dynamics in the data, even for diminishing signal-to-noise ratios. Hence, by cycling their training with data assimilation [54, 55], generative surrogates have a huge potential to learn unknown physics from observations.

The most common strategy for Earth system modelling is to have models for each Earth system component which interact through coupling. Yet, this strategy can fail for AI-based component models: as we have demonstrated, the dynamics of these models show an entanglement between components, here sea ice and the ocean. This makes it challenging to isolate the dynamics of a single component due to external forcings from other components. Therefore, we have to rethink how to do coupled Earth system modelling, when using AI-based models.

4 Methods

4.1 Data used for GenSIM

The model is trained and compared to a 24-year-long simulation (1995-2018) [36] produced by neXtSIM [5], an advanced sea-ice model employing Lagrangian finite elements and a brittle Bingham-Maxwell rheology [6] (data available at https://github.com/sasip-climate/catalog-shared-data-SASIP/blob/main/outputs/OPA-neXtSIM_CREG025-ILBOXE140.md, last access: 18th August 2025). For this simulation, neXtSIM has been coupled to OPA, the ocean component of the NEMO modelling framework [37] and has been forced with the ERA5 reanalysis [45] for the atmosphere. The curvilinear mesh of our model corresponds to the Eulerian Arakawa-C mesh of OPA, to which the model output of neXtSIM has been interpolated. GenSIM predicts the sea-ice thickness, concentration, damage, u - and v -velocity, and the snow-on-ice thickness. All variables but the damage are averaged in a six hour window, while the damage is an instantaneous state.

In addition to the initial conditions, GenSIM takes external atmospheric forcings from the ERA5 reanalysis dataset [45]. Originally on a latitude-longitude mesh with a $1/4^\circ$ resolution, the dataset is interpolated to our curvilinear mesh by nearest neighbour. The forcings consist of the 2-metre temperature, the 2-metre specific humidity, the 10-metre equatorial and meridional wind velocities. The specific humidity is estimated from the 2-metre temperature, 2-metre dew point, and surface pressure.

To obtain neural network inputs that contain a memory about the past development without having access to the ocean, we construct degree day features from the 2-metre temperature [56, 57]. Using a temperature threshold of $T_{\text{thres}} = 271.35$ K, we construct the positive, PDD , and negative degree days, NDD , by

$$PDD(T_{2m}, \Delta t) = \int_{t-\Delta t}^t \text{maximum}(T_{2m}(s) - T_{\text{thres}}, 0) ds$$

$$\text{and } NDD(T_{2m}, \Delta t) = \int_{t-\Delta t}^t \text{minimum}(T_{2m}(s) - T_{\text{thres}}, 0) ds,$$

respectively. To extract seasonal and yearly features, we use a six-hourly integration resolution with two windows into the past, $\Delta t = 30$ days and $\Delta t = 366$ days. This results in four additional forcing features per forecast time, leading to 12 forcing inputs in total (four forcings for two time steps and four degree day features).

4.2 Evaluation data

We evaluate our long-term simulation with the sea-ice–ocean reanalysis product from the Pan-Arctic Ice-Ocean Modeling and Assimilation System (PIOMAS) [49] (data available at <https://psc.apl.uw.edu/research/projects/arctic-sea-ice-volume-anomaly>, last access: 18th August 2025). The here used dataset is on a one-degree latitudinal-longitudinal mesh and consists of monthly averaged sea-ice thickness and concentration values.

The sea-ice volume is additionally evaluated with the CS2/SMOS product [50] (Version 2.6, data available at <https://spaces.awi.de/spaces/CS2SMOS/overview>, last access: 18th August 2025), which merges satellite observations from the CryoSat2 and Soil Moisture and Ocean Salinity (SMOS) missions. As CS2/SMOS infers solely the sea-ice thickness, it is complemented by sea-ice concentration observations of the EUMETSAT’s climate data record from the OSISAF project [58], which merges satellite measurements from SSMR, SSM/I, and SSMIS. Both datasets are on the EASE mesh with 25 km resolution.

The deformation rates from the sea-ice dynamics are evaluated with the Lagrangian data from the RADARSAT Geophysical Processing System (RGPS) [59] (data available at <https://asf.alaska.edu/datasets/daac/sea-ice-measures>, last access: 18th August 2025). This dataset tracks features between two successive Synthetic Aperture Radar (SAR) images and provides high-resolution sea-ice motion data at a typical 10 km spatial resolution and a time resolution of around three days.

4.3 Surrogate modelling with censored flow matching

In the following, we expose the most important equations to understand how GenSIM and the deterministic model are trained. For a more rigorous treatment and a mathematical derivation of the equations, we refer to Appendix B.

For a forecast window of 12 hours, based on the current state \mathbf{x}_t and the forcings in the same window $\mathbf{F}_{t:t+12\text{h}}$, the surrogate model should predict the sea-ice state $\mathbf{x}_{t+12\text{h}}$ —consisting of sea-ice thickness, concentration, damage, the velocities in

x - and y -direction, and the snow-on-ice thickness. Instead of predicting the future state directly, the model outputs predicted tendencies $\widehat{\mathbf{z}}$, which are scaled by the per-variable climatological standard deviation of the tendencies σ_{clim} such that we can recover the prediction by

$$\widehat{\mathbf{x}}_{t+12\text{h}} = \mathbf{x}_t + \sigma_{\text{clim}}\widehat{\mathbf{z}}. \quad (1)$$

In our autoregressive framework, the subsequent prediction $\widehat{\mathbf{x}}_{t+24\text{h}}$ is performed with the previous prediction and updated forcings $\mathbf{F}_{t+12\text{h}:t+24\text{h}}$ as new inputs. This way, we can extend the prediction as long as possible [28, 60].

For training, we have access to a training dataset with data triplets $(\mathbf{x}_t, \mathbf{x}_{t+12\text{h}}, \mathbf{F}_{t:t+12\text{h}}) \sim \mathcal{D}$. From these data triplets, we can construct the targetted tendencies, $\mathbf{z} = (\mathbf{x}_{t+12\text{h}} - \mathbf{x}_t)/\sigma_{\text{clim}}$.

The deterministic model directly predicts the normalised tendencies with a neural network and its weights and biases θ , $\widehat{\mathbf{z}}_{\text{det}} = g_{\theta}(\mathbf{x}_t, \mathbf{F}_{t:t+12\text{h}})$. The loss function of the deterministic model is then simply the mean-squared error between the output and the targetted tendencies,

$$\mathcal{L}_{\text{det}}(\theta) = \mathbb{E}_{\mathcal{D}} [\|\mathbf{z} - g_{\theta}(\mathbf{x}_t, \mathbf{F}_{t:t+12\text{h}})\|_2^2], \quad (2)$$

where we take the norm over all variables and all unmasked grid points. As we work in normalised tendency space, the loss function automatically weights the different state variables by the reciprocal of their standard deviation, $1/(\sigma_{\text{clim}})^2$, as similarly used for other deterministic surrogate models [35, 60].

For GenSIM, we instantiate a generative flow to produce stochastic predictions [24, 48]. The generative flow is defined by the integration of an ordinary differential equation (ODE) in pseudo time $\tau \in [0, 1]$,

$$\frac{d\mathbf{z}_{\tau}}{d\tau} = \mathbf{u} \quad (3)$$

with its velocity \mathbf{u} and the initial conditions at pseudo time $\tau = 0$,

$$\mathbf{z}_0 \sim \mathcal{N}(\mathbf{0}, \mathbf{I}). \quad (4)$$

Note that the subscript τ describes the dependency on the pseudo time, whereas t is the real time.

During training, when we know the targetted tendencies, we construct a linear interpolant [25] connecting the known tendencies to a sample from the initial conditions,

$$\mathbf{z}_{\tau} = \tau\mathbf{z} + (1 - \tau)\mathbf{z}_0. \quad (5)$$

The analytical velocity, as the pseudo-time derivative of the linear interpolant, is constant in time and reads

$$\mathbf{u} = \mathbf{z} - \mathbf{z}_0. \quad (6)$$

However, this velocity is only known during training, and we use a trained neural network as approximation for predictions such that $\mathbf{u} \approx \widehat{\mathbf{v}}_{\theta}(\mathbf{z}_{\tau}, \mathbf{x}_t, \mathbf{F}_{t:t+12\text{h}}, \tau)$ should hold.

Based on variational flow matching [44], the commonly used loss function is reparametrised to account for an appropriate bounding of the sea-ice states with \mathbf{x}^L as lower bound and \mathbf{x}^U as upper bound. For this reparametrisation, we introduce a new per-variable standard deviation \mathbf{s} which specifies the expected uncertainty of the neural network’s velocity approximation and is used as learnable weighting [61]. As the true flow is a linear interpolant, we can make a mean-field approximation, factorising the loss function over the $n_{\text{vars}} = 6$ variables and n_{grid} unmasked grid points,

$$\mathcal{L}_{\text{GenSIM}}(\boldsymbol{\theta}, \mathbf{s}) = \mathbb{E}_{\tau, \mathbf{z}_0, \mathcal{D}} \left[\sum_{k=1}^{n_{\text{vars}}} \sum_{l=1}^{n_{\text{grid}}} J(\boldsymbol{\theta}, \mathbf{s}, k, l) \right]. \quad (7)$$

Using a censored Gaussian as variational distribution [34], we obtain as component cost function,

$$\begin{aligned} J(\boldsymbol{\theta}, \mathbf{s}, k, l) = & \mathbf{I}(x_k^L < x_{t+12\text{h},k,l} < x_k^U) \left[\frac{1}{2 \cdot (s_k)^2} (u_{k,l} - \hat{v}_{\boldsymbol{\theta},k,l})^2 + \log(s_k) \right] \\ & - \mathbf{I}(x_{t+12\text{h},k,l} = x_k^L) \left[\log \Phi \left(\frac{u_{k,l} - \hat{v}_{\boldsymbol{\theta},k,l}}{s_k} \right) \right] \\ & - \mathbf{I}(x_{t+12\text{h},k,l} = x_k^U) \left[\log \Phi \left(\frac{\hat{v}_{\boldsymbol{\theta},k,l} - u_{k,l}}{s_k} \right) \right] \end{aligned} \quad (8)$$

with Φ as the normal Gaussian cumulative distribution function (CDF), $\mathbf{I}(\cdot)$ as indicator function, and $(\cdot)_{k,l}$ as scalar that is indexed for the k -th variable and the l -th grid point. Note that the case for the cost function is changed depending on the true state at time $t + 12$ h, which differs from the common practise of using activation functions for the bounds during training. For variables that are unbounded like the velocities, the lower and upper bound vanish and only the weighted mean-squared error is left as cost function. When the true state is between the physical bounds, the cost function is the commonly used one for flow matching [23, 24], where the prediction target is the true velocity. When the true state is exactly on the lower or upper bound, the prediction is pushed towards exceeding these bounds in negative or positive direction, respectively. Hence, this cost function effectively modifies the role of the predicted velocity: it regresses the true velocity and classifies if the lower or upper bound is reached.

The censored Gaussian distribution can be derived from applying a static thresholding function [43] to the prediction that follows a Gaussian distribution and, hence, properly accounts for physical bounding in that predictions. To apply the neural network’s output as velocity approximation, we have to project the states to $\tau = 1$ and apply the thresholding,

$$\hat{\mathbf{z}}_{1|\tau} = \text{minimum} \left(\text{maximum}(\mathbf{z}_\tau + \tau \hat{\mathbf{v}}_{\boldsymbol{\theta}}, (\mathbf{x}^L - \mathbf{x}_t) / \sigma_{\text{clim}}), (\mathbf{x}^U - \mathbf{x}_t) / \sigma_{\text{clim}} \right) \quad (9)$$

with $\text{minimum}(\cdot, \cdot)$ and $\text{maximum}(\cdot, \cdot)$ as minimum and maximum function, respectively. Based on this thresholded state, we recover the thresholded velocity by the

relation

$$\widehat{\mathbf{v}}_{\theta} = \frac{\widehat{\mathbf{z}}_{1|\tau} - \mathbf{z}_{\tau}}{1 - \tau}, \quad (10)$$

which can be used in any integration scheme to solve the ODE that defines the generative flow, Eq. (3). Effectively, we treat the neural network’s output as median approximation for the velocity, which is thresholded if the bounds are exceeded. This way, we can generate data that lies exactly on possible bounds, while being produced by a deterministic velocity approximation.

4.4 Experimental details

In our experiments, we train two different surrogate models: GenSIM and a deterministic baseline model. To make both models comparable, we use similar experimental settings, which we explain in the following.

GenSIM is based on a transformer architecture, as concisely described in Section 1 and further elucidated in Appendix C.1. Since the transformer scales quadratically with the number of grid points/tokens, we use a U-ViT architecture [34, 35, 62] for the deterministic model: a convolutional U-Net coarse-grains the pan-Arctic data, while we use a transformer in the bottleneck with almost the same configuration as for GenSIM. Due to the additional convolutional blocks, the deterministic model is with 32.2×10^6 parameters slightly bigger than GenSIM with 28.1×10^6 parameters. To counteract the increased tendency to overfit by the deterministic model, we use the model that performs the best over the validation dataset.

The neural networks are trained with Eq. (7) and Eq. (2) for GenSIM and the deterministic model, respectively. The dataset for both models is augmented by distribution augmentation [35, 47], where the data is randomly flipped in horizontal and vertical direction, and randomly rotated by a 90° angle. The labels, describing which augmentation is activated, are added to the input of the neural networks.

GenSIM is trained with pseudo time steps drawn from a uniform distribution, $\tau \in U(0, 1)$, while the weighting of the loss function is learned alongside the model [63], effectively reducing the need to tune the training of the generative flow. The samples are randomly averaged with window sizes drawn from (1, 2, 4, 8) with probabilities (0.533, 0.266, 0.133, 0.066) and randomly sliced into patches with 80×80 grid points such that each patch contains at least 10% unmasked grid points. For the estimation of the loss function, we remove the 8-pixel border around each patch to obtain a prediction size of 64×64 . In total, we randomly extract eight patches per sample for GenSIM’s training.

Both models are trained with mini-batches of 32 samples and the AdamW optimiser [64, 65] with $\beta_1 = 0.9$ and $\beta_2 = 0.99$ and a weight decay with $\lambda = 10^{-3}$. The learning rate is linearly increased from $\gamma_{\min} = 10^{-6}$ to $\gamma_{\max} = 5 \times 10^{-4}$ within the first 5000 iterations. Afterwards, the learning rate is decayed by a cosine until the end of the training: 1×10^6 iterations for GenSIM and 5×10^5 iterations for the deterministic model. After training, we retain the model that has the lowest validation loss: GenSIM reaches its optimum at the end, while the deterministic model starts to overfit after around 1.5×10^5 iterations. We track the exponential moving average (EMA) of the model’s weights with a decay rate of $\alpha = 0.9999$. We train the models on data for

1995–2014, giving 913 iterations per training epoch, while we validate on 2015. The testing period 2016–2018 is only revealed after the training has been finished and used to produce the results in this study.

We train on two Nvidia RTX A6000 with 48 GB memory (per-device batch size 16) and eight Nvidia A100 with 80 GB memory (per-device batch size 4). The training of GenSIM needs on the eight Nvidia A100 around 2 days. The models are implemented with *bfloat16* mixed-precision in Python [66] based on PyTorch [67], PyTorch lightning [68], and Hydra [69]. The data and code for the models will be made publicly available upon acceptance.

As sampler for GenSIM, we use a second-order Heun scheme [61] with 20 steps and a sigmoid-like pseudo-time scheduler as visualised in Fig. B4b. Each forecast with GenSIM hence needs 39 neural network evaluations, taking around 4.5 s on a Nvidia RTX A6000.

4.5 Comparison between GenSIM and deterministic model

For the testing period, 2016–2018, we produce weekly forecasts with GenSIM and the deterministic model. Starting from 1st January of each year, we initialise 10-day forecasts on a weekly basis, performing 153 initialisations in total. The forecasts are initialised with the state from neXtSIM-OPA and use forcings from the ERA5 reanalysis. We run an ensemble with 16 members for GenSIM, while we run a single forecast per initialisation for the deterministic model. These forecasts are then compared to the neXtSIM-OPA simulation as truth.

We evaluate the root-mean-squared error (RMSE) between the forecasts and the truth over all ocean grid points that are covered by sea ice in the neXtSIM-OPA simulation (concentration > 0.15). To estimate a normalised RMSE, we normalise the forecast errors by the standard deviation of the climatology. The spread-skill ratio is estimated as ratio between the root-mean-squared standard deviation from GenSIM’s ensemble members and the RMSE of the ensemble mean with a correction factor of $\sqrt{17/16}$ [70].

The energy spectra are estimated over the central Arctic region with 128×128 grid points and averaged in logarithmic space over all initialisation times. To estimate the extent accuracy, the predicted sea-ice concentration is converted into an extent mask (concentration > 0.15). The accuracy is then the agreement between the prediction and the truth over all ocean grid points.

4.6 Sea-ice volume estimation

We normalise all sea-ice volume datasets into a common format: we use the Cartesian EASE-25-km mesh from CS2/SMOS as common mesh on which the volumes are estimated. We interpolate the sea-ice thickness and concentration of each dataset with bilinear interpolation to that mesh.

Additionally, we create a common sea-ice mask: for each original dataset, we map its land-sea mask onto the common mesh. In addition to these land-sea masks, we interpolate the climatological EASE-12.5-km mask (available at <ftp://osisaf.met.no/>

reprocessed/ice/oceanmasks/, last access: 18th August, 2025) to the common mesh, retaining only cells where sea ice was observed in the climatology.

The PIOMAS dataset has a monthly temporal resolution. Hence, we average all sea-ice thicknesses and concentrations to the monthly resolution, before we estimate their product. The sea-ice volume is then the product between sea-ice thickness, sea-ice concentration and cell area (25 km \times 25 km).

4.7 Scaling analysis of sea-ice deformation rates

Since GenSIM has been trained on data up to 2014, we split the analysis of the sea-ice deformation rates into two parts: in the first part, we track individual features found by RGPS in the GenSIM and neXtSIM simulations for a qualitative analysis. In the second part, we work on the common curvilinear mesh of GenSIM and neXtSIM, using spatial averaging for a quantitative scaling analysis.

The individual features found by RGPS are grouped with a 12-hourly frequency from 2007-02-01 03:00 to 2007-02-10 15:00 with a ± 6 h window. From this grouped dataset, we retain only features that are far from the coast (≥ 150 km) and are refound three days later. Based on the temporal and spatial difference, we estimate the velocity of the features by the relation $\mathbf{u}_t = (\mathbf{x}_{t+3d} - \mathbf{x}_t)/\Delta t$, where $\Delta t \in (2d + 12h, 3d + 12h)$ is the true time difference.

Afterwards, we triangulate each group of features, retaining triangles with all angles larger than 20° and an area between 25 km^2 and 400 km^2 . The velocity gradients, needed to estimate the deformation rates, are estimated based on the found triangles with the contour integral [9], e.g., $u_x = \frac{1}{A} \oint u dy$ for the u -velocity gradient in x -direction with A as triangle area. The shear deformation, $\dot{\epsilon}_{\text{shear}}$, divergent deformation, $\dot{\epsilon}_{\text{div}}$, and total deformation rates $\dot{\epsilon}_{\text{tot}}$ are estimated by

$$\dot{\epsilon}_{\text{shear}} = \sqrt{(u_x - v_y)^2 + (u_y + v_x)^2}, \quad (11)$$

$$\dot{\epsilon}_{\text{div}} = u_x + v_y, \quad (12)$$

$$\text{and } \dot{\epsilon}_{\text{tot}} = \sqrt{\dot{\epsilon}_{\text{shear}}^2 + \dot{\epsilon}_{\text{div}}^2}. \quad (13)$$

Every 12-hours, we initialise particles at positions of the found features. Based on the simulated velocity, we advect all particles three-days forward in time for the GenSIM and neXtSIM simulation. As advection scheme, we use a simple forward Euler integration with an hourly time step, a bilinear velocity interpolation in space, and linear interpolation in time. The displacement of the particle within the three days determines then the velocity.

To make a quantitative analysis from 2015-01-01 03:00 to 2018-12-31 15:00, we use the central Arctic slice (see also Fig. A1) of GenSIM's $1/4^\circ$ mesh, circumventing issues with land masses. Instead of advecting particles, we calculate the velocity gradients with the predicted velocities, which correspond to six-hourly averages. The velocity gradients are given by the contour integral over the rectangles that are defined by four neighbouring cells. We estimate the deformation rates based on the velocity gradients as before with Eq. (11)–(13).

As similarly used in other studies [6], we coarse-grain the velocity gradients by area-averaging over increasing window size. The coarse-grained velocity then provide us with deformation rates at that coarse-graining scale. At each scale, we track the first three distributional moments of the deformation rates. The scaling analysis in space assumes that the moments q follow a power law, $\langle \dot{\epsilon}^q(L) \rangle \sim L^{-\beta(q)}$, which depends on the spatial resolution L . The scaling coefficient $\beta(q)$ describes how the moments change by coarse-graining. The dependence of the scaling coefficients on the moment gives an estimate how much the localisation of fracturing events are dependent on the magnitude of these events, a positive curvature indicates thereby a multifractal behaviour [9].

4.8 Estimation of sea-ice volume change

The change in the sea-ice volume, vol_t , is presumably driven by dynamics (advection) and other sources, S_t , among which are growing and melting because of thermodynamics,

$$\frac{\partial \text{vol}_t}{\partial t} + \nabla \cdot (\mathbf{u}_t \text{vol}_t) = S_t. \quad (14)$$

To estimate the sea-ice volume change, we use finite differences, $\frac{\partial \text{vol}_t}{\partial t} \approx (\text{vol}_{t+12\text{h}} - \text{vol}_t)/12\text{h}$. Working on the Arakawa-C mesh, we further approximate the dynamical part with a second-order centred finite-volume advection scheme based on the volume and velocities for time t and assume constant dynamics until time $t + 12\text{h}$. The source term S_t is then given as difference between the true volume change and the change explained by the approximated dynamics.

Acknowledgements. This study is a contribution to the SASIP project funded under Grant no. *G-24-66154* by Schmidt Science—a philanthropic initiative that seeks to improve societal outcomes through the development of emerging science and technologies. TSF, MB, CD, and AF additionally received financial support from INSU/CNRS by the project DeepGeneSIS (PNTS). This work was granted access to the HPC resources of IDRIS under the allocations 2021-AD011013069, 2022-AD011013069R1, 2023-AD011013069R2, and 2024-AD011013069R3 made by GENCI. We would like to thank Lorenzo Zampieri and Joffrey Dumont Le Brazidec (ECMWF), through discussing they helped to focus this study. Additionally, we acknowledge Guillaume Boutin (NERSC) for providing the training dataset and other members from the SASIP project which gave helpful comments along the way. This work contains data modified from Copernicus Climate Change Service information 2024. Neither the European Commission nor ECMWF is responsible for any use that may be made of the Copernicus information or data it contains. CEREIA is a member of the Institut Pierre-Simon Laplace (IPSL).

References

- [1] Marsan, D., Stern, H., Lindsay, R., Weiss, J.: Scale Dependence and Localization of the Deformation of Arctic Sea Ice. *Physical Review Letters* **93**(17), 178501 (2004) <https://doi.org/10.1103/PhysRevLett.93.178501>

- [2] Rampal, P., Weiss, J., Marsan, D., Lindsay, R., Stern, H.: Scaling properties of sea ice deformation from buoy dispersion analysis. *Journal of Geophysical Research: Oceans* **113**(C3), 2007–004143 (2008) <https://doi.org/10.1029/2007JC004143>
- [3] Hibler, W.D.: A Dynamic Thermodynamic Sea Ice Model. *Journal of Physical Oceanography* **9**(4), 815–846 (1979) [https://doi.org/10.1175/1520-0485\(1979\)009<0815:ADTSIM>2.0.CO;2](https://doi.org/10.1175/1520-0485(1979)009<0815:ADTSIM>2.0.CO;2). Chap. *Journal of Physical Oceanography*
- [4] Dansereau, V., Weiss, J., Saramito, P., Lattes, P.: A Maxwell elasto-brittle rheology for sea ice modelling. *The Cryosphere* **10**(3), 1339–1359 (2016) <https://doi.org/10.5194/tc-10-1339-2016>
- [5] Rampal, P., Bouillon, S., Ólason, E., Morlighem, M.: neXtSIM: A new Lagrangian sea ice model. *The Cryosphere* **10**(3), 1055–1073 (2016) <https://doi.org/10.5194/tc-10-1055-2016>
- [6] Ólason, E., Boutin, G., Korosov, A., Rampal, P., Williams, T., Kimmritz, M., Dansereau, V., Samaké, A.: A New Brittle Rheology and Numerical Framework for Large-Scale Sea-Ice Models. *Journal of Advances in Modeling Earth Systems* **14**(8), 2021–002685 (2022) <https://doi.org/10.1029/2021MS002685>
- [7] Brodeau, L., Rampal, P., Ólason, E., Dansereau, V.: Implementation of a brittle sea ice rheology in an Eulerian, finite-difference, C-grid modeling framework: Impact on the simulated deformation of sea ice in the Arctic. *Geoscientific Model Development* **17**(15), 6051–6082 (2024) <https://doi.org/10.5194/gmd-17-6051-2024>
- [8] Ólason, E., Boutin, G., Williams, T., Korosov, A., Regan, H., Rheinländer, J., Rampal, P., Flocco, D., Samaké, A., Davy, R., Spain, T., Chua, S.: The next generation sea-ice model neXtSIM, version 2. *EGUsphere*, 1–33 (2025) <https://doi.org/10.5194/egusphere-2024-3521>
- [9] Rampal, P., Dansereau, V., Olason, E., Bouillon, S., Williams, T., Korosov, A., Samaké, A.: On the multi-fractal scaling properties of sea ice deformation. *The Cryosphere* **13**(9), 2457–2474 (2019) <https://doi.org/10.5194/tc-13-2457-2019>
- [10] Bouchat, A., Hutter, N., Chanut, J., Dupont, F., Dukhovskoy, D., Garric, G., Lee, Y.J., Lemieux, J.-F., Lique, C., Losch, M., Maslowski, W., Myers, P.G., Ólason, E., Rampal, P., Rasmussen, T., Talandier, C., Tremblay, B., Wang, Q.: Sea Ice Rheology Experiment (SIREx): 1. Scaling and Statistical Properties of Sea-Ice Deformation Fields. *Journal of Geophysical Research: Oceans* **127**(4), 2021–017667 (2022) <https://doi.org/10.1029/2021JC017667>
- [11] Samaké, A., Rampal, P., Bouillon, S., Ólason, E.: Parallel implementation of a Lagrangian-based model on an adaptive mesh in C++: Application to sea-ice. *Journal of Computational Physics* **350**, 84–96 (2017) <https://doi.org/10.1016/j.jcp.2017.08.055>

- [12] Durand, C., Finn, T.S., Farchi, A., Bocquet, M., Boutin, G., Ólason, E.: Data-driven surrogate modeling of high-resolution sea-ice thickness in the Arctic. *The Cryosphere* **18**(4), 1791–1815 (2024) <https://doi.org/10.5194/tc-18-1791-2024>
- [13] Andersson, T.R., Hosking, J.S., Pérez-Ortiz, M., Paige, B., Elliott, A., Russell, C., Law, S., Jones, D.C., Wilkinson, J., Phillips, T., Byrne, J., Tietsche, S., Sarojini, B.B., Blanchard-Wrigglesworth, E., Aksenov, Y., Downie, R., Shuckburgh, E.: Seasonal Arctic sea ice forecasting with probabilistic deep learning. *Nature Communications* **12**(1), 5124 (2021) <https://doi.org/10.1038/s41467-021-25257-4>
- [14] Liu, Q., Zhang, R., Wang, Y., Yan, H., Hong, M.: Daily Prediction of the Arctic Sea Ice Concentration Using Reanalysis Data Based on a Convolutional LSTM Network. *Journal of Marine Science and Engineering* **9**(3), 330 (2021) <https://doi.org/10.3390/jmse9030330>
- [15] Kvanum, A.F., Palerme, C., Müller, M., Rabault, J., Hughes, N.: Developing a deep learning forecasting system for short-term and high-resolution prediction of sea ice concentration. *EGU sphere*, 1–26 (2024) <https://doi.org/10.5194/egusphere-2023-3107>
- [16] Kochkov, D., Yuval, J., Langmore, I., Norgaard, P., Smith, J., Mooers, G., Klöwer, M., Lottes, J., Rasp, S., Düben, P., Hatfield, S., Battaglia, P., Sanchez-Gonzalez, A., Willson, M., Brenner, M.P., Hoyer, S.: Neural general circulation models for weather and climate. *Nature* **632**(8027), 1060–1066 (2024) <https://doi.org/10.1038/s41586-024-07744-y>
- [17] Subich, C., Husain, S.Z., Separovic, L., Yang, J.: Fixing the Double Penalty in Data-Driven Weather Forecasting through a Modified Spherical Harmonic Loss Function. *arXiv* (2025). <https://doi.org/10.48550/arXiv.2501.19374>
- [18] Bonavita, M.: On Some Limitations of Current Machine Learning Weather Prediction Models. *Geophysical Research Letters* **51**(12), 2023–107377 (2024) <https://doi.org/10.1029/2023GL107377>
- [19] Parthipan, R., Anand, M., Christensen, H.M., Hosking, J.S., Wischik, D.J.: Defining Error Accumulation in ML Atmospheric Simulators. *arXiv* (2024). <https://doi.org/10.48550/arXiv.2405.14714>
- [20] Chattopadhyay, A., Sun, Y.Q., Hassanzadeh, P.: Challenges of Learning Multi-Scale Dynamics with AI Weather Models: Implications for Stability and One Solution. *arXiv* (2024). <https://doi.org/10.48550/arXiv.2304.07029>
- [21] Sohl-Dickstein, J., Weiss, E.A., Maheswaranathan, N., Ganguli, S.: Deep Unsupervised Learning using Nonequilibrium Thermodynamics. *arXiv:1503.03585 [cond-mat, q-bio, stat]* (2015) [arXiv:1503.03585](https://arxiv.org/abs/1503.03585) [cond-mat, q-bio, stat]
- [22] Song, Y., Sohl-Dickstein, J., Kingma, D.P., Kumar, A., Ermon, S., Poole, B.:

- Score-Based Generative Modeling through Stochastic Differential Equations. arXiv (2021). <https://doi.org/10.48550/arXiv.2011.13456>
- [23] Liu, X., Gong, C., Liu, Q.: Flow Straight and Fast: Learning to Generate and Transfer Data with Rectified Flow. arXiv (2022). <https://doi.org/10.48550/arXiv.2209.03003>
- [24] Lipman, Y., Chen, R.T.Q., Ben-Hamu, H., Nickel, M., Le, M.: Flow Matching for Generative Modeling. arXiv (2023). <https://doi.org/10.48550/arXiv.2210.02747>
- [25] Albergo, M.S., Boffi, N.M., Vanden-Eijnden, E.: Stochastic Interpolants: A Unifying Framework for Flows and Diffusions. arXiv (2023). <https://doi.org/10.48550/arXiv.2303.08797>
- [26] Li, L., Carver, R., Lopez-Gomez, I., Sha, F., Anderson, J.: SEEDS: Emulation of Weather Forecast Ensembles with Diffusion Models. arXiv (2023). <https://doi.org/10.48550/arXiv.2306.14066>
- [27] Finn, T.S., Disson, L., Farchi, A., Bocquet, M., Durand, C.: Representation learning with unconditional denoising diffusion models for dynamical systems. *Nonlinear Processes in Geophysics* **31**(3), 409–431 (2024) <https://doi.org/10.5194/npg-31-409-2024>
- [28] Price, I., Sanchez-Gonzalez, A., Alet, F., Andersson, T.R., El-Kadi, A., Masters, D., Ewalds, T., Stott, J., Mohamed, S., Battaglia, P., Lam, R., Willson, M.: Probabilistic weather forecasting with machine learning. *Nature* **637**(8044), 84–90 (2025) <https://doi.org/10.1038/s41586-024-08252-9>
- [29] Mardani, M., Brenowitz, N., Cohen, Y., Pathak, J., Chen, C.-Y., Liu, C.-C., Vahdat, A., Nabian, M.A., Ge, T., Subramaniam, A., Kashinath, K., Kautz, J., Pritchard, M.: Residual Corrective Diffusion Modeling for Km-Scale Atmospheric Downscaling. arXiv (2024). <https://doi.org/10.48550/arXiv.2309.15214>
- [30] Meuer, J., Witte, M., Finn, T.S., Timmreck, C., Ludwig, T., Kadow, C.: Latent Diffusion Model for Generating Ensembles of Climate Simulations. arXiv (2024). <https://doi.org/10.48550/arXiv.2407.02070>
- [31] Cachay, S.R., Henn, B., Watt-Meyer, O., Bretherton, C.S., Yu, R.: Probabilistic Emulation of a Global Climate Model with Spherical Diffusion. arXiv (2024). <https://doi.org/10.48550/arXiv.2406.14798>
- [32] Brenowitz, N.D., Ge, T., Subramaniam, A., Gupta, A., Hall, D.M., Mardani, M., Vahdat, A., Kashinath, K., Pritchard, M.S.: Climate in a Bottle: Towards a Generative Foundation Model for the Kilometer-Scale Global Atmosphere (2025)
- [33] Xu, J., Tu, S., Yang, W., Li, S., Liu, K., Luo, Y., Ma, L., Fei, B., Bai, L.: IceDiff: High Resolution and High-Quality Sea Ice Forecasting with Generative Diffusion

- Prior. arXiv (2024). <https://doi.org/10.48550/arXiv.2410.09111>
- [34] Finn, T.S., Durand, C., Farchi, A., Bocquet, M., Brajard, J.: Towards Diffusion Models for Large-Scale Sea-Ice Modelling. arXiv (2024). <https://doi.org/10.48550/arXiv.2406.18417>
- [35] Finn, T.S., Durand, C., Farchi, A., Bocquet, M., Rampal, P., Carrassi, A.: Generative Diffusion for Regional Surrogate Models From Sea-Ice Simulations. *Journal of Advances in Modeling Earth Systems* **16**(10), 2024–004395 (2024) <https://doi.org/10.1029/2024MS004395>
- [36] Boutin, G., Ólason, E., Rampal, P., Regan, H., Lique, C., Talandier, C., Brodeau, L., Ricker, R.: Arctic sea ice mass balance in a new coupled ice–ocean model using a brittle rheology framework. *The Cryosphere* **17**(2), 617–638 (2023) <https://doi.org/10.5194/tc-17-617-2023>
- [37] Madec, G., Bell, M., Blaker, A., Bricaud, C., Bruciaferri, D., Castrillo, M., Calvert, D., Jérôme Chanut, Clementi, E., Coward, A., Epicoco, I., Éthé, C., Ganderton, J., Harle, J., Hutchinson, K., Iovino, D., Lea, D., Lovato, T., Martin, M., Martin, N., Mele, F., Martins, D., Masson, S., Mathiot, P., Mocavero, S., Müller, S., Nurser, A.J.G., Paronuzzi, S., Peltier, M., Person, R., Rousset, C., Rynders, S., Samson, G., Téchené, S., Vancoppenolle, M., Wilson, C.: NEMO Ocean Engine Reference Manual (2023) <https://doi.org/10.5281/zenodo.8167700>
- [38] England, M.R., Polvani, L.M., Screen, J., Chan, A.C.: Minimal arctic sea ice loss in the last 20 years, consistent with internal climate variability. *Geophysical Research Letters* **52**(15), 2025–116175 (2025) <https://doi.org/10.1029/2025GL116175>
- [39] Zhang, Q., Song, J., Huang, X., Chen, Y., Liu, M.-Y.: DiffCollage: Parallel Generation of Large Content with Diffusion Models. In: 2023 IEEE/CVF Conference on Computer Vision and Pattern Recognition (CVPR), pp. 10188–10198 (2023). <https://doi.org/10.1109/CVPR52729.2023.00982>
- [40] Peebles, W., Xie, S.: Scalable Diffusion Models with Transformers. arXiv (2023). <https://doi.org/10.48550/arXiv.2212.09748>
- [41] Vaswani, A., Shazeer, N., Parmar, N., Uszkoreit, J., Jones, L., Gomez, A.N., Kaiser, L., Polosukhin, I.: Attention Is All You Need. arXiv:1706.03762 [cs] (2017) [arXiv:1706.03762](https://arxiv.org/abs/1706.03762) [cs]
- [42] Heo, B., Park, S., Han, D., Yun, S.: Rotary Position Embedding for Vision Transformer. arXiv (2024). <https://doi.org/10.48550/arXiv.2403.13298>
- [43] Saharia, C., Chan, W., Saxena, S., Li, L., Whang, J., Denton, E.L., Ghasemipour, K., Gontijo Lopes, R., Karagol Ayan, B., Salimans, T., Ho, J., Fleet, D.J.,

- Norouzi, M.: Photorealistic Text-to-Image Diffusion Models with Deep Language Understanding. *Advances in Neural Information Processing Systems* **35**, 36479–36494 (2022)
- [44] Eijkelboom, F., Bartosh, G., Naeseth, C.A., Welling, M., van de Meent, J.-W.: Variational Flow Matching for Graph Generation. arXiv (2024). <https://doi.org/10.48550/arXiv.2406.04843>
- [45] Hersbach, H., Bell, B., Berrisford, P., Hirahara, S., Horányi, A., Muñoz-Sabater, J., Nicolas, J., Peubey, C., Radu, R., Schepers, D., Simmons, A., Soci, C., Abdalla, S., Abellan, X., Balsamo, G., Bechtold, P., Biavati, G., Bidlot, J., Bonavita, M., De Chiara, G., Dahlgren, P., Dee, D., Diamantakis, M., Dragani, R., Flemming, J., Forbes, R., Fuentes, M., Geer, A., Haimberger, L., Healy, S., Hogan, R.J., Hólm, E., Janisková, M., Keeley, S., Laloyaux, P., Lopez, P., Lupu, C., Radnoti, G., De Rosnay, P., Rozum, I., Vamborg, F., Villaume, S., Thépaut, J.-N.: The ERA5 global reanalysis. *Quarterly Journal of the Royal Meteorological Society* **146**(730), 1999–2049 (2020) <https://doi.org/10.1002/qj.3803>
- [46] Wang, Z., Jiang, Y., Zheng, H., Wang, P., He, P., Wang, Z., Chen, W., Zhou, M.: Patch diffusion: Faster and more data-efficient training of diffusion models. In: *Proceedings of the 37th International Conference on Neural Information Processing Systems. NeurIPS '23*, pp. 72137–72154. Curran Associates Inc., Red Hook, NY, USA (2024)
- [47] Jun, H., Child, R., Chen, M., Schulman, J., Ramesh, A., Radford, A., Sutskever, I.: Distribution Augmentation for Generative Modeling. In: *Proceedings of the 37th International Conference on Machine Learning*, pp. 5006–5019. PMLR, Vienna, Austria (2020)
- [48] Couairon, G., Singh, R., Charantonis, A., Lessig, C., Monteleoni, C.: ArchesWeather & ArchesWeatherGen: A Deterministic and Generative Model for Efficient ML Weather Forecasting. arXiv (2024). <https://doi.org/10.48550/arXiv.2412.12971>
- [49] Zhang, J., Rothrock, D.A.: Modeling global sea ice with a thickness and enthalpy distribution model in generalized curvilinear coordinates. *Monthly Weather Review* **131**(5), 845–861 (2003) [https://doi.org/10.1175/1520-0493\(2003\)131<0845:MGSIIWA>2.0.CO;2](https://doi.org/10.1175/1520-0493(2003)131<0845:MGSIIWA>2.0.CO;2) . Chap. *Monthly Weather Review*
- [50] Ricker, R., Hendricks, S., Kaleschke, L., Tian-Kunze, X., King, J., Haas, C.: A weekly arctic sea-ice thickness data record from merged CryoSat-2 and SMOS satellite data. *The Cryosphere* **11**(4), 1607–1623 (2017) <https://doi.org/10.5194/tc-11-1607-2017>
- [51] Sumata, H., De Steur, L., Divine, D.V., Granskog, M.A., Gerland, S.: Regime shift in Arctic Ocean sea ice thickness. *Nature* **615**(7952), 443–449 (2023) <https://doi.org/10.1038/s41586-022-05686-x>

- [52] Mohammadi-Aragh, M., Goessling, H.F., Losch, M., Hutter, N., Jung, T.: Predictability of arctic sea ice on weather time scales. *Scientific Reports* **8**(1), 6514 (2018) <https://doi.org/10.1038/s41598-018-24660-0>
- [53] Durand, C., Finn, T.S., Farchi, A., Bocquet, M., Brajard, J., Bertino, L.: Four-dimensional variational data assimilation with a sea-ice thickness emulator. *EGUsphere*, 1–36 (2025) <https://doi.org/10.5194/egusphere-2024-4028>
- [54] Bocquet, M., Brajard, J., Carrassi, A., Bertino, L.: Bayesian inference of chaotic dynamics by merging data assimilation, machine learning and expectation-maximization. *Foundations of Data Science* **2**(1), 55 (2020) <https://doi.org/10.3934/fods.2020004> [arXiv:2001.06270](https://arxiv.org/abs/2001.06270) [physics, stat]
- [55] Rozet, F., Andry, G., Lanusse, F., Louppe, G.: Learning diffusion priors from observations by expectation maximization. *Advances in Neural Information Processing Systems* **37**, 87647–87682 (2024)
- [56] Leppäranta, M.: A review of analytical models of sea-ice growth. *Atmosphere-Ocean* **31**(1), 123–138 (1993) <https://doi.org/10.1080/07055900.1993.9649465>
- [57] Braithwaite, R.J.: Positive degree-day factors for ablation on the greenland ice sheet studied by energy-balance modelling. *Journal of Glaciology* **41**(137), 153–160 (1995) <https://doi.org/10.3189/S0022143000017846>
- [58] EUMETSAT Ocean and Sea Ice Satellite Application Facility: Global Sea Ice Concentration Climate Data Record 1978-2020 (2025). https://doi.org/10.15770/EUM_SAF_OSL0023
- [59] Kwok, R., Schweiger, A., Rothrock, D.A., Pang, S., Kottmeier, C.: Sea ice motion from satellite passive microwave imagery assessed with ERS SAR and buoy motions. *Journal of Geophysical Research: Oceans* **103**(C4), 8191–8214 (1998) <https://doi.org/10.1029/97JC03334>
- [60] Lam, R., Sanchez-Gonzalez, A., Willson, M., Wirnsberger, P., Fortunato, M., Alet, F., Ravuri, S., Ewalds, T., Eaton-Rosen, Z., Hu, W., Merose, A., Hoyer, S., Holland, G., Vinyals, O., Stott, J., Pritzel, A., Mohamed, S., Battaglia, P.: Learning skillful medium-range global weather forecasting. *Science* **382**(6677), 1416–1421 (2023) <https://doi.org/10.1126/science.adi2336>
- [61] Karras, T., Aittala, M., Lehtinen, J., Hellsten, J., Aila, T., Laine, S.: Analyzing and Improving the Training Dynamics of Diffusion Models. *arXiv* (2023). <https://doi.org/10.48550/arXiv.2312.02696>
- [62] Hoogeboom, E., Heek, J., Salimans, T.: Simple Diffusion: End-to-end Diffusion for High Resolution Images. *arXiv* (2023). <https://doi.org/10.48550/arXiv.2301.11093>

- [63] Karras, T., Aittala, M., Aila, T., Laine, S.: Elucidating the Design Space of Diffusion-Based Generative Models. arXiv (2022). <https://doi.org/10.48550/arXiv.2206.00364>
- [64] Kingma, D.P., Ba, J.: Adam: A Method for Stochastic Optimization. arXiv:1412.6980 [cs] (2017) [arXiv:1412.6980](https://arxiv.org/abs/1412.6980) [cs]
- [65] Loshchilov, I., Hutter, F.: Decoupled Weight Decay Regularization. arXiv (2019). <https://doi.org/10.48550/arXiv.1711.05101>
- [66] Van Rossum, G.: Python tutorial, Technical Report CS-R9526. Technical report, Centrum voor Wiskunde en Informatica (CWI), Amsterdam (May 1995)
- [67] Paszke, A., Gross, S., Massa, F., Lerer, A., Bradbury, J., Chanan, G., Killeen, T., Lin, Z., Gimelshein, N., Antiga, L., Desmaison, A., Kopf, A., Yang, E., DeVito, Z., Raison, M., Tejani, A., Chilamkurthy, S., Steiner, B., Fang, L., Bai, J., Chintala, S.: Pytorch: An imperative style, high-performance deep learning library. In: Advances in Neural Information Processing Systems 32, pp. 8024–8035. Curran Associates, Inc., Red Hook, NY, USA (2019)
- [68] Falcon, W., Borovec, J., Wälchli, A., Eggert, N., Schock, J., Jordan, J., Skafte, N., IridXD, Bereznyuk, V., Harris, E., Murrell, T., Yu, P., Præsius, S., Addair, T., Zhong, J., Lipin, D., Uchida, S., Bapat, S., Schröter, H., Dayma, B., Karnachev, A., Kulkarni, A., Komatsu, S., Martin.B, SCHIRATTI, J.-B., Mary, H., Byrne, D., Eyzaguirre, C., cinjon, Bakhtin, A.: PyTorchLightning: 0.7.6 Release. Zenodo (2020). <https://doi.org/10.5281/zenodo.3828935>
- [69] Yadan, O.: Hydra - A Framework for Elegantly Configuring Complex Applications. Github (2019)
- [70] Fortin, V., Abaza, M., Anctil, F., Turcotte, R.: Why Should Ensemble Spread Match the RMSE of the Ensemble Mean? *Journal of Hydrometeorology* **15**(4), 1708–1713 (2014) <https://doi.org/10.1175/JHM-D-14-0008.1> . Chap. *Journal of Hydrometeorology*
- [71] Meier, W., Stewart, J.: Arctic and Antarctic Regional Masks for Sea Ice and Related Data Products, Version 1. NASA National Snow and Ice Data Center Distributed Active Archive Center (2023). <https://doi.org/10.5067/CYW308ZUNIWC>
- [72] Lam, R., Sanchez-Gonzalez, A., Willson, M., Wirnsberger, P., Fortunato, M., Alet, F., Ravuri, S., Ewalds, T., Eaton-Rosen, Z., Hu, W., Merose, A., Hoyer, S., Holland, G., Vinyals, O., Stott, J., Pritzel, A., Mohamed, S., Battaglia, P.: GraphCast: Learning Skillful Medium-Range Global Weather Forecasting. arXiv (2023). <https://doi.org/10.48550/arXiv.2212.12794>
- [73] Lang, S., Alexe, M., Chantry, M., Dramsch, J., Pinault, F., Raoult, B., Clare,

- M.C.A., Lessig, C., Maier-Gerber, M., Magnusson, L., Bouallègue, Z.B., Nemesio, A.P., Dueben, P.D., Brown, A., Pappenberger, F., Rabier, F.: AIFS - ECMWF's Data-Driven Forecasting System. arXiv (2024). <https://doi.org/10.48550/arXiv.2406.01465>
- [74] Batzolis, G., Stanczuk, J., Schönlieb, C.-B., Etmann, C.: Conditional Image Generation with Score-Based Diffusion Models. arXiv (2021). <https://doi.org/10.48550/arXiv.2111.13606>
- [75] Cipolla, R., Gal, Y., Kendall, A.: Multi-task Learning Using Uncertainty to Weigh Losses for Scene Geometry and Semantics. In: 2018 IEEE/CVF Conference on Computer Vision and Pattern Recognition, pp. 7482–7491. IEEE, Salt Lake City, UT, USA (2018). <https://doi.org/10.1109/CVPR.2018.00781>
- [76] Kingma, D.P., Gao, R.: Understanding Diffusion Objectives as the ELBO with Simple Data Augmentation. arXiv (2023). <https://doi.org/10.48550/arXiv.2303.00848>
- [77] Chen, T., Zhang, R., Hinton, G.: Analog Bits: Generating Discrete Data Using Diffusion Models with Self-Conditioning. arXiv (2023). <https://doi.org/10.48550/arXiv.2208.04202>
- [78] Lou, A., Ermon, S.: Reflected Diffusion Models. In: Proceedings of the 40th International Conference on Machine Learning, pp. 22675–22701. PMLR, Honolulu, Hawaii, USA (2023)
- [79] Fishman, N., Klarner, L., Bortoli, V.D., Mathieu, E., Hutchinson, M.J.: Diffusion models for constrained domains. Transactions on Machine Learning Research (2023)
- [80] Tobin, J.: Estimation of Relationships for Limited Dependent Variables. *Econometrica* **26**(1), 24 (1958) <https://doi.org/10.2307/1907382>
- [81] Amemiya, T.: Regression Analysis when the Dependent Variable Is Truncated Normal. *Econometrica* **41**(6), 997 (1973) <https://doi.org/10.2307/1914031>
- [82] Crowson, K., Baumann, S.A., Birch, A., Abraham, T.M., Kaplan, D.Z., Shippole, E.: Scalable High-Resolution Pixel-Space Image Synthesis with Hourglass Diffusion Transformers. In: Forty-First International Conference on Machine Learning (2024)
- [83] Rahimi, A., Recht, B.: Random features for large-scale kernel machines. In: Advances in Neural Information Processing Systems, vol. 20. Curran Associates, Inc., Red Hook, NY, USA (2007)
- [84] Hendrycks, D., Gimpel, K.: Gaussian Error Linear Units (Gelus). arXiv (2016).

<https://doi.org/10.48550/arXiv.1606.08415>

- [85] He, K., Zhang, X., Ren, S., Sun, J.: Deep Residual Learning for Image Recognition. arXiv:1512.03385 [cs] (2015) [arXiv:1512.03385](https://arxiv.org/abs/1512.03385) [cs]
- [86] Zhang, B., Sennrich, R.: Root Mean Square Layer Normalization. arXiv (2019). <https://doi.org/10.48550/arXiv.1910.07467>
- [87] Su, J., Ahmed, M., Lu, Y., Pan, S., Bo, W., Liu, Y.: RoFormer: Enhanced transformer with Rotary Position Embedding. *Neurocomputing* **568**, 127063 (2024) <https://doi.org/10.1016/j.neucom.2023.127063>
- [88] Shazeer, N.: GLU Variants Improve Transformer. arXiv (2020). <https://doi.org/10.48550/arXiv.2002.05202>
- [89] Ronneberger, O., Fischer, P., Brox, T.: U-Net: Convolutional Networks for Biomedical Image Segmentation. arXiv:1505.04597 [cs] (2015) [arXiv:1505.04597](https://arxiv.org/abs/1505.04597) [cs]
- [90] Chen, G., Zhao, X., Zhou, Y., Qu, X., Chen, T., Cheng, Y.: Towards Stabilized and Efficient Diffusion Transformers through Long-Skip-Connections with Spectral Constraints. arXiv (2025). <https://doi.org/10.48550/arXiv.2411.17616>
- [91] Shi, W., Caballero, J., Huszár, F., Totz, J., Aitken, A.P., Bishop, R., Rueckert, D., Wang, Z.: Real-Time Single Image and Video Super-Resolution Using an Efficient Sub-Pixel Convolutional Neural Network. arXiv (2016). <https://doi.org/10.48550/arXiv.1609.05158>
- [92] Liu, G., Reda, F.A., Shih, K.J., Wang, T.-C., Tao, A., Catanzaro, B.: Image Inpainting for Irregular Holes Using Partial Convolutions. In: *Proceedings of the European Conference on Computer Vision (ECCV)*, pp. 85–100 (2018)
- [93] Liu, Z., Mao, H., Wu, C.-Y., Feichtenhofer, C., Darrell, T., Xie, S.: A ConvNet for the 2020s. arXiv (2022)

Appendix A RMSE Score cards

Inspired by ECMWF’s score cards (<https://sites.ecmwf.int/ifs/scorecards/>, last access: 19th August 2025), the root-mean-squared error is decomposed into averages across seasons and regions. For that decomposition, we use the indexed regions as indicated in Fig. A1. Mesh cells over the Atlantic ocean that mostly cover open water are omitted from the estimation of the root-mean-squared error (RMSE). As previously, the RMSE is estimated only over ice-covered mesh cells (concentration > 0.15). The score cards (Fig. A2 and Fig. A3) show how GenSIM’s ensemble mean improves the predictions compared to the deterministic surrogate model. Note that there is almost no snow during summer (JAS), making its error estimate unreliable in that season.

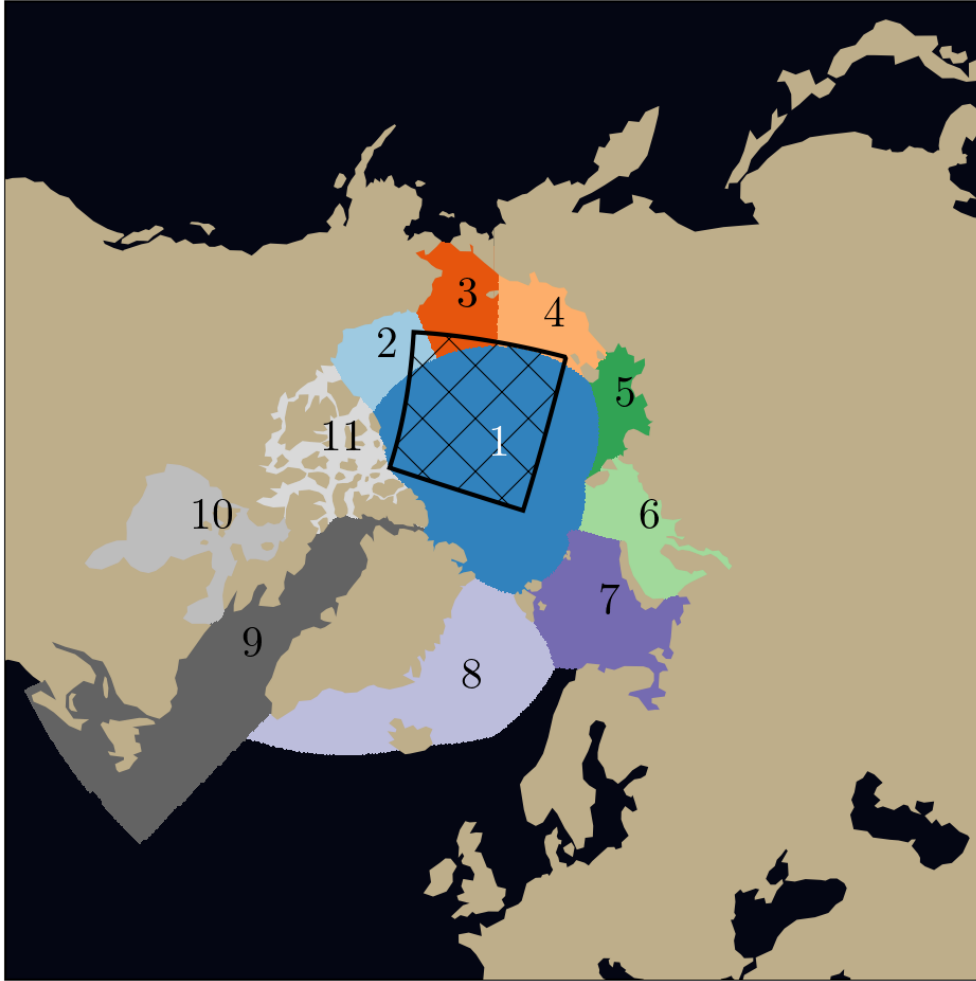


Fig. A1 The different regions used throughout the manuscript with the following names: 1=central Arctic; 2=Beaufort sea; 3=Chukchi sea; 4=east Siberian sea; 5=Laptev sea; 6=Kara sea; 7=Barents sea; 8=east Greenland sea; 9=Baffin bay, Labrador seas, and gulf of St. Lawrence; 10=Hudson bay; 11=Canadian archipelago. The black hatched rectangle is the region in the central Arctic used to estimate the spectra and fractal scaling. The regions are extracted from NSIDC's regions on the EASE-Grid 2.0 with a 3.125 km resolution [71].

Across all seasons and all regions, GenSIM's ensemble mean shows a persistent improvement in the RMSE compared to the deterministic surrogate model. However, when sea ice starts to refreeze during autumn (OND), GenSIM's sea-ice concentration forecast has apparently some issues, which lead to a degradation of the forecasts over lead times of several days, generally impacting the scores for the sea-ice concentration. Potentially, a tuning of the sampling scheduling for GenSIM could remedy this degradation.

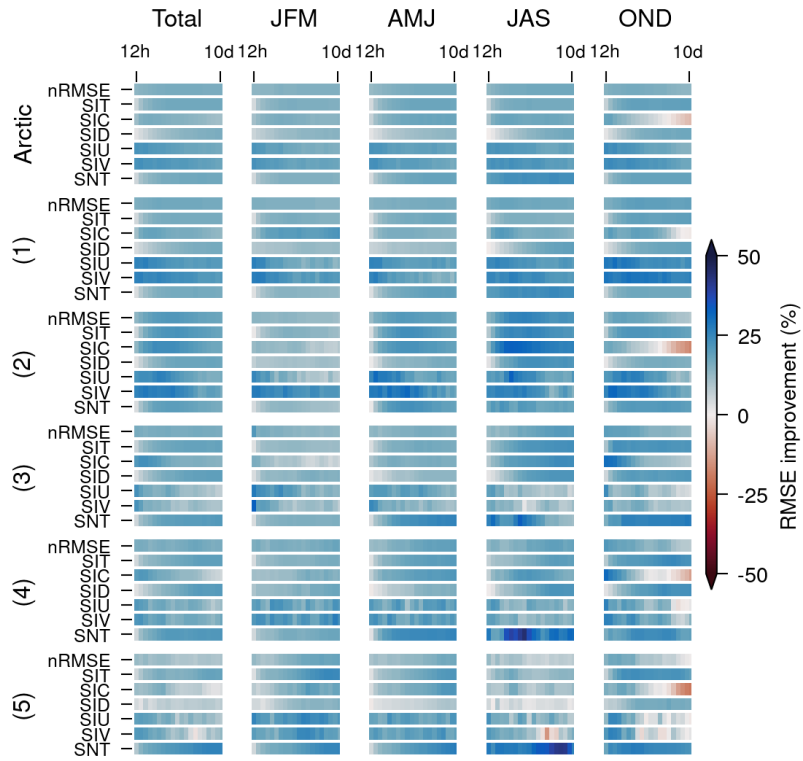


Fig. A2 The score card, depicting the relative root-mean-squared error (RMSE) of GenSIM's ensemble mean to the RMSE of the deterministic baseline for different regions, variables, and seasons, as estimated over all ice-covered grid points (sit=thickness, sic=concentration, sid=damage, siu= u -velocity, siv= v -velocity, snt=snow-on-ice thickness). A blue RMSE corresponds to an improvement of GenSIM, while a red one shows a degradation of the forecast. The regions (1–5) are depicted and explained in Fig. A1 and remaining regions are shown in Fig. A3.

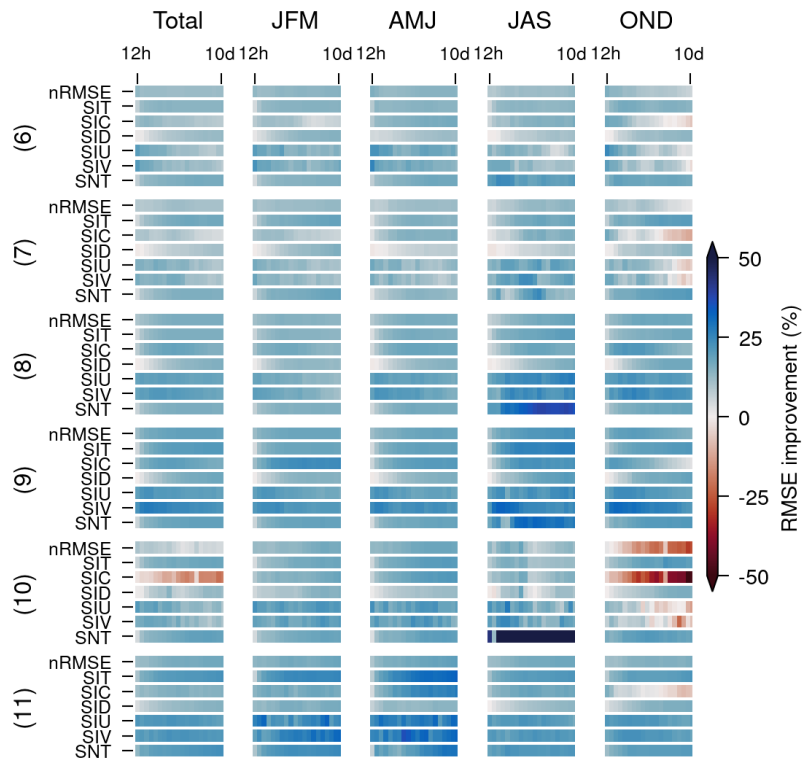


Fig. A3 Continuation of Fig. A2 for regions (6–11).

Appendix B Mathematical framework for surrogate modelling

Our goal is to develop a powerful surrogate model that forecasts sea-ice states with a 12-hour lead time, $\mathbf{x}_{t+12\text{h}}$, given some initial states \mathbf{x}_t and external forcings $\mathbf{F}_{t:t+12\text{h}}$ provided at initial time t and 12 hours later, $t + 12\text{h}$. As a reminder, the predictive variables are the sea-ice thickness, the concentration, the damage, the two velocity components, and the snow-on-ice thickness. Our model predicts the tendency within the 12 hours,

$$\mathbf{x}_{t+12\text{h}} \approx \widehat{\mathbf{x}}_{\theta,t+12\text{h}} = \mathbf{x}_t + \mathcal{M}_{\theta}(\mathbf{x}_t, \mathbf{F}_{t:t+12\text{h}}), \quad (\text{B1})$$

with $\widehat{\mathbf{x}}_{\theta,t+12\text{h}}$ as the model prediction. The tendency model $\mathcal{M}_{\theta}(\cdot)$ is based on a deep neural network with its learnable weights and biases θ . Here, we train two different types of models: a deterministic model [12] and a generative model based on flow matching [23–25].

To train the models, we sample data triplets from a training dataset $(\mathbf{x}_t, \mathbf{x}_{t+12\text{h}}, \mathbf{F}_{t:t+12\text{h}}) \sim \mathcal{D}$ and minimise the loss functions using variants of stochastic gradient descent. Once trained, we employ the models as outlined in Eq. (B1) to propagate the initial states forward and to generate a 12-hour lead time prediction. For predictions extending beyond 12 hours, we utilise the model autoregressively, wherein the preceding prediction serves as the input for the subsequent time step, with the forcings being updated accordingly.

In practice, states are processed in a normalised space, in which the output of the neural network is scaled. The latent state that the neural network outputs reads

$$\mathbf{z} = \frac{\mathbf{x}_{t+12\text{h}} - \mathbf{x}_t}{\sigma_{\text{clim}}}. \quad (\text{B2})$$

The normalisation factor $1/\sigma_{\text{clim}}$ is the reciprocal of the per-variable climatological standard deviation, estimated over all training samples and all unmasked ocean grid points. To recover the prediction, we can scale and add the output to the initial states, $\widehat{\mathbf{x}}_{t+12\text{h}} = \mathbf{x}_t + \sigma_{\text{clim}}\widehat{\mathbf{z}}$.

B.1 Deterministic model

The deterministic model is trained to predict the mean of an assumed Gaussian distribution as a single outcome, conditioned on the initial states and forcings. For the autoregressive prediction, the mean is treated as point estimate, which is reused as input for the next time step.

For training, we assume that true sea-ice state after 12 hours is drawn from a Gaussian distribution with the prediction as the mean and a constant diagonal covariance matrix,

$$\mathbf{x}_{t+12\text{h}} \sim \mathcal{N}(\widehat{\mathbf{x}}_{\theta,t+12\text{h}}, \sigma_{\text{clim}}^2 \mathbf{I}), \quad (\text{B3})$$

with the values on the diagonal of the covariance as the vector of all climatological standard deviations. Using maximum likelihood estimation for the predicted mean,

the corresponding loss function is a weighted mean-squared error,

$$\mathcal{L}_{\text{det}}(\boldsymbol{\theta}) = \mathbb{E}_{\mathcal{D}} [\mathbf{w} \|\mathbf{x}_{t+12\text{h}} - \widehat{\mathbf{x}}_{\boldsymbol{\theta}, t+12\text{h}}\|_2^2], \quad (\text{B4})$$

with $\mathbf{w} = 1/\sigma_{\text{clim}}^2$ as weighting vector. This loss function is commonly used for other surrogate models [12, 72, 73] and serves as a baseline for our generative model.

In normalised space, the loss function reduces equivalently to a mean-squared error between the targetted latent variable and the predicted latent variable, as the weighting is subsumed into the normalisation,

$$\mathcal{L}_{\text{det}}(\boldsymbol{\theta}) = \mathbb{E}_{\mathcal{D}} [\|\mathbf{z} - \widehat{\mathbf{z}}_{\boldsymbol{\theta}}\|_2^2]. \quad (\text{B5})$$

This underlines the role of the climatological standard deviation in the deterministic model: it is used as scaling for the output of the neural network but also as weighting in the loss function.

B.2 Generative flows for surrogate modelling

While the deterministic model predicts a single outcome, our goal with a model based on generative flows is to produce a valid sample from the predictive probability distribution through refinement. Starting from common flow matching, we derive this refinement process, and we further introduce the concepts needed for the loss functions to train the generative model. In the end, we will derive censored flow matching as a way to constrain the resulting generative flow by physical bounds.

B.2.1 Probabilistic predictions with flow matching

In our flow matching model, the latent state \mathbf{z}_{τ} is evolved in pseudo time τ from pure noise at $\tau = 0$ to a sample from the targetted distribution at $\tau = 1$. Note that the latent state is dependent on the pseudo time τ as denoted by its subscript, while the true sea-ice state depends on real time t . The prior distribution of the latent state is a Gaussian with zero mean and identity covariance,

$$\mathbf{z}_0 \sim \mathcal{N}(\mathbf{0}, \mathbf{I}). \quad (\text{B6})$$

During training, the targetted distribution is known through samples, $\mathbf{z}_1 = (\mathbf{x}_{t+12\text{h}} - \mathbf{x})/\sigma_{\text{clim}}$, as previously.

The ordinary differential equation (ODE) that governs the generative flow in normalised space is given by

$$\frac{d\mathbf{z}_{\tau}}{d\tau} = \mathbf{u}(\mathbf{z}_{\tau}), \quad (\text{B7})$$

where $\mathbf{u}(\mathbf{z}_{\tau})$ represents the velocity of the flow. When the velocity is known, we can integrate the ODE in pseudo-time and produce new data samples.

For training, the flow is constructed by a linear interpolant,

$$\mathbf{z}_{\tau} = \tau \mathbf{z}_1 + (1 - \tau) \mathbf{z}_0, \quad (\text{B8})$$

resulting in a constant true velocity independent of \mathbf{z}_τ and τ ,

$$\mathbf{u} = \mathbf{z}_1 - \mathbf{z}_0. \quad (\text{B9})$$

Since \mathbf{z}_1 is targetted and the analytical velocity therefore unknown during prediction, we train the neural network with its parameters $\boldsymbol{\theta}$ to approximate the true velocity, $\mathbf{u} \approx \widehat{\mathbf{v}}_{\boldsymbol{\theta}}(\mathbf{z}, \tau, \mathbf{x}_t, \mathbf{F}_{t:t+12h})$. By conditioning the approximation on the initial states and forcings, the neural network learns to sample from the conditional distribution [74].

To train the neural network, we draw mini-batches of samples for the pseudo time $\tau \in [0, 1]$ and the prior $\mathbf{z}_0 \sim \mathcal{N}(\mathbf{0}, \mathbf{I})$ in addition to the initial and targetted states, and forcings. After constructing the latent states $\mathbf{z}_\tau, \mathbf{z}_1$, the following loss function is minimised:

$$\mathcal{L}_{\text{FM}}(\boldsymbol{\theta}) = \mathbb{E}_{\tau, \mathbf{z}_0, \mathcal{D}} [\|\mathbf{u} - \widehat{\mathbf{v}}_{\boldsymbol{\theta}}(\mathbf{z}_\tau, \tau, \mathbf{x}_t, \mathbf{F}_{t:t+12h})\|_2^2]. \quad (\text{B10})$$

Once trained, we can employ the neural network as velocity approximation for the ODE, Equation (B7). By initialising with Equation (B6) and integrating the ODE in pseudo time from $\tau = 0$ to $\tau = 1$, we produce a sample from the target distribution, conditioned on the initial states and forcings. By drawing different initialisations, an ensemble of predictions can be produced from the same conditional information. In practise, we perform the integration with a second-order Heun scheme [63] in 20 steps, where the discrete steps are scheduled with a shifted sigmoid function, as shown in Fig. B4b.

Notably, if projected back into physical space, the generative flow is initialised by a sample from the prior distribution around the initial conditions $\mathcal{N}(\mathbf{x}_t, \boldsymbol{\sigma}_{\text{clim}}^2 \mathbf{I})$ and maps to a sample from the predictive distribution for \mathbf{x}_{t+12h} . Although a deterministic forecast, trained with Equation (B4), could also be used to define the prior [29, 48], previous work [35] has demonstrated negligible performance difference, and we therefore employ a persistence forecast as prior for simplicity. Since the integration of the ODE maps from the initial conditions to the prediction, it works similarly to classical geophysical models [27], integrating in pseudo time instead of real time. Hence, we can make use of established numerical tools to render generative flow models more efficient and to scale them up, e.g., by domain decomposition.

B.2.2 Variational flow matching

To obtain further insights in how flow matching works and lay the ground for further concepts, we describe variational flow matching [44] in the following. In the end, we demonstrate that flow matching can be seen as a generalisation of the deterministic model that refines the predictions instead of making a one-step projection.

Variational flow matching predicts the variational distribution of terminal states $q_{\boldsymbol{\theta}}(\mathbf{z}_1 | \mathbf{z}_\tau)$ instead of a point estimate for the velocity. We can connect these two by

$$\mathbf{v}_{\boldsymbol{\theta}}(\mathbf{z}_\tau, \tau) = \mathbb{E}_{\mathbf{z}_1 \sim q_{\boldsymbol{\theta}}(\mathbf{z}_1 | \mathbf{z}_\tau)} [\mathbf{u}(\mathbf{z}_\tau | \mathbf{z}_1)]. \quad (\text{B11})$$

The conditional velocity $\mathbf{u}(\mathbf{z}_\tau | \mathbf{z}_1)$ is obtained from the linear interpolation, Equation (B8),

$$\mathbf{u}(\mathbf{z}_\tau | \mathbf{z}_1) = \frac{\mathbf{z}_1 - \mathbf{z}_\tau}{1 - \tau}. \quad (\text{B12})$$

Since this conditional velocity is analytically defined, the approximated velocity, Equation (B11), matches the true velocity, if the variational distribution matches the true distribution $p(\mathbf{z}_1 | \mathbf{z}_\tau)$, which suggests a minimisation of the Kullback-Leibler divergence between these two distributions as loss function,

$$\begin{aligned}\mathcal{L}_{\text{VFM}}(\boldsymbol{\theta}) &= \mathbb{E}_\tau \left[D_{\text{KL}} \left(p(\mathbf{z}_\tau) p(\mathbf{z}_1 | \mathbf{z}_\tau) \parallel p(\mathbf{z}_\tau) q_\theta(\mathbf{z}_1 | \mathbf{z}_\tau) \right) \right] \\ &= -\mathbb{E}_{t, \mathbf{z}_0, \mathcal{D}} \left[\log (q_\theta(\mathbf{z}_1 | \mathbf{z}_\tau)) \right] + C,\end{aligned}\tag{B13}$$

where C represents terms that do not depend on $\boldsymbol{\theta}$. Thanks to a mean-field approximation [44], the log-likelihood can further be factorised over the n_{vars} variables and the n_{grid} grid points to

$$\mathcal{L}_{\text{VFM}}(\boldsymbol{\theta}) = -\mathbb{E}_{t, \mathbf{z}_0, \mathcal{D}} \left[\sum_{k=1}^{n_{\text{vars}}} \sum_{l=1}^{n_{\text{grid}}} \log (q_\theta(z_{1,k,l} | \mathbf{z}_\tau)) \right] + C\tag{B14}$$

with $z_{1,k,l}$ as the terminal state for the k -th variable and l -th grid point.

Variational flow matching is a generalisation of the previously stated flow matching. The linearity of the conditional velocity allows us to reduce the variational distribution to a mean-field approximation, where the distribution over all variables and grid points is factorised. By combining mean-field variational flow matching with a Gaussian assumption, we recover conventional flow matching up to a constant [44],

$$q_\theta(\mathbf{z}_1 | \mathbf{z}_\tau) = \mathcal{N}(\hat{\boldsymbol{\mu}}_\theta, (1 - \tau)^2 \mathbf{I})\tag{B15}$$

with

$$\hat{\boldsymbol{\mu}}_\theta = \mathbf{z}_\tau + (1 - \tau) \hat{\mathbf{v}}_\theta(\mathbf{z}, \tau, \mathbf{x}_t, \mathbf{F}_{t:t+12h}).\tag{B16}$$

The covariance, $(1 - \tau)^2 \mathbf{I}$, is chosen such that the scaling of the mean-squared error vanishes,

$$\begin{aligned}\mathcal{L}_{\text{VFM}}(\boldsymbol{\theta}) &= \mathbb{E}_{\tau, \mathbf{z}_0, \mathcal{D}} \left[\frac{1}{2} \frac{1}{(1 - \tau)^2} \|\boldsymbol{\mu}_{\text{truth}} - \hat{\boldsymbol{\mu}}_\theta\|_2^2 + C_1 \right] \\ &= \mathbb{E}_{\tau, \mathbf{z}_0, \mathcal{D}} \left[\frac{1}{2(1 - \tau)^2} \|(1 - \tau)\mathbf{v} - (1 - \tau)\hat{\mathbf{v}}_\theta(\mathbf{z}, \tau, \mathbf{x}_t, \mathbf{F}_{t:t+12h})\|_2^2 \right] + C_2 \\ &\propto \mathbb{E}_{\tau, \mathbf{z}_0, \mathcal{D}} \left[\|\mathbf{v} - \hat{\mathbf{v}}_\theta(\mathbf{z}, \tau, \mathbf{x}_t, \mathbf{F}_{t:t+12h})\|_2^2 \right],\end{aligned}\tag{B17}$$

with $\boldsymbol{\mu}_{\text{truth}} = \mathbf{z}_\tau + (1 - \tau)\mathbf{v}$ and the constants C_1 and C_2 , which do not depend on $\boldsymbol{\theta}$. Hence, flow matching still adheres to a Gaussian assumption for the predictions, like the deterministic model. Yet, its covariance diminishes through the successive refinements, yielding a sample from the targeted probability distribution.

An interesting case arises when we employ the model with a single step, mapping directly from $\tau = 0$ to $\tau = 1$: there, the latent state for $\tau = 0$ contains no information about the prediction. Consequently, if a neural network is trained for that, it would learn to disregard the latent state as input and to target a mean prediction [23],

similar to the deterministic model. In this case, the model effectively reduces to a deterministic prediction model.

B.2.3 Learnable uncertainty weighting

The weighting in the loss function for the deterministic model and flow matching is determined by the climatological standard deviation. However, each of the six predicted variables is subject to distinct physical processes, leading to varying degrees of predictability; for example, the velocities are generally easier to predict than the thickness, which might be not captured by their climatological weighting [75].

We account for this in a data-dependent weighting by altering the Gaussian assumption of variational flow matching, Equation (B15), and making some covariances learnable. As a simplification and exploiting the mean-field approximation, we introduce a per-variable standard deviation that depends on the pseudo time, $\mathbf{s}(\tau)$, obtaining

$$q_{\theta}(\mathbf{z}_1 | \mathbf{z}_{\tau}) = \mathcal{N}\left(\hat{\boldsymbol{\mu}}_{\theta}, \frac{1}{2}\left((1-\tau) \cdot \mathbf{s}(\tau)\right)^2 \mathbf{I}\right), \quad (\text{B18})$$

as variational distribution. The corresponding loss function for flow matching reads

$$\mathcal{L}_{\text{VFM}}(\boldsymbol{\theta}, \mathbf{s}) = \mathbb{E}_{\tau, \mathbf{z}_0, \mathcal{D}} \left[\frac{1}{2 \cdot (\mathbf{s}(\tau))^2} \|\mathbf{u} - \hat{\mathbf{v}}_{\theta}(\mathbf{z}, \tau, \mathbf{x}_t, \mathbf{F}_{t:t+12h})\|_2^2 + \log(\mathbf{s}(\tau)) \right], \quad (\text{B19})$$

which has a similar formulation for diffusion models [61]. The squared standard deviation, $(\mathbf{s}(\tau))^2$, converges to half of the expected per-variable mean-squared error of the velocity and adapts automatically to the predictability of different variables.

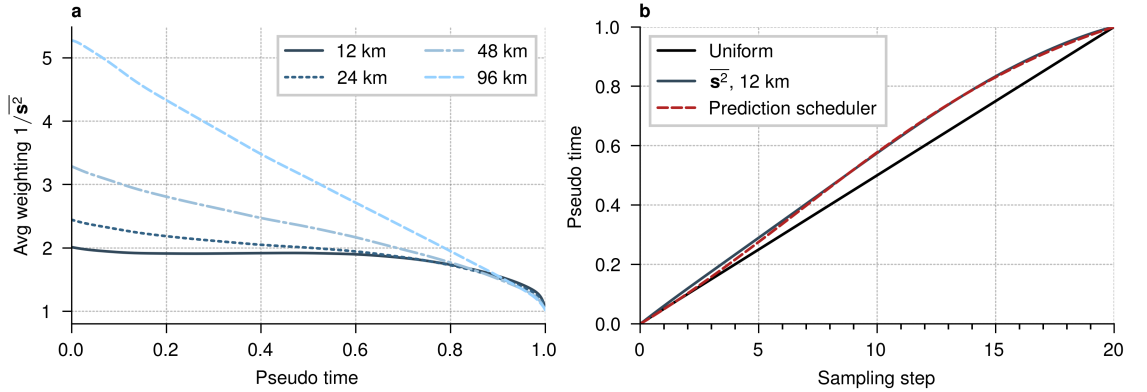


Fig. B4 Learned weighting of the flow matching loss (a) The learned weighting, averaged across all six variables, at different resolutions indicates the importance of difference scales at different resolutions. (b) Used in an importance-sampling-like mechanism, the learned standard deviation can guide the tuning of the pseudo time scheduler during prediction. Here, the focus is on smaller scales, as opposed to a uniform scheduler.

Note that, while the weighting in the loss function is learned, the output of the neural network is still scaled by the climatological standard deviation. This disentanglement between the scaling and the learned weighting becomes especially interesting when the neural network is trained across different datasets or resolutions: we can set a constant scaling of the neural network and learn different weightings per dataset (Fig. B4a). The weighting concentrates around the relevant scales, acting as gradient normalisation and stabilising the training [61].

This learnable weighting can reduce the need to tune the scheduler during training and prediction. We can also use the learned standard deviation to guide our inference scheduler (Fig. B4b). The larger the learned standard deviation, the larger the expected error for that scale, and importance sampling suggests that we should oversample these scales [76]. Hence, we want to concentrate our pseudo time scheduler during prediction to the scales where the expected error is large, which are in our case the small scales. While these small scales might be unimportant for perceptual generation like images, they can become especially important when the model is auto-regressively cycled, as errors at small scales can amplify over time and impact larger scales. As prediction scheduler, we use a shifted sigmoid weighting, $\tau_i = \sigma(\alpha \cdot (\frac{i}{20} - 0.5) + \beta)$ with $\alpha = 3$ and $\beta = 0.5$, which we normalise into the range $\tau_0 = 0$ and $\tau_1 = 1$. This scheduler shifts integration steps at intermediate scales towards smaller scales, increasing the importance therein.

B.2.4 Censored flow matching for physical bounds

Sea-ice states are inherently bounded: sea-ice and snow thickness are non-negative, while sea-ice concentration and damage are limited between 0 and 1. Furthermore, the absence of sea ice (zero thickness) implies a lack of motion. We hypothesise that explicitly incorporating these physical priors will improve the prediction accuracy.

Static thresholding, where the predictions are clipped into its physical bounds, can enforce these bounds [43]. However, models trained with the mean-squared error are biased and prone to spurious fluctuations near these boundaries [77]. These fluctuations can be particularly problematic in autoregressive predictions, where they may amplify instabilities in long-term simulations. Generative flow models that incorporate bounds via reflection or log-barriers [78, 79] enforce a bound-avoiding behaviour such that the bound is never reached, leading to unphysical predictions, where, e.g., all grid points exhibit sea ice, similar to a truncated distribution approximation. Instead, we introduce censored flow matching, accounting for static thresholding during training.

In censoring, all predictions that exceed a bound are exactly mapped to that bound. We generally assume that there exist true sea-ice dynamics without physical bounds, e.g., in the tropics, sea ice would still melt even though no sea ice is observed there. When the observed data is censored to a bound, its dynamics are unknown, and we have just the information that the dynamics exceeded the bound. In this case, the approximated velocity should increase the probability that the reproduced prediction exceeds the bound as well. To achieve this, we use the predicted velocity to estimate an approximated cumulative distribution function (CDF) from the variational Gaussian distribution. The CDF is then evaluated at the bounded velocity, and its logarithm

replaces the mean-squared error loss for censored data points. A visualisation of the targetted training process is shown in Fig. B5.

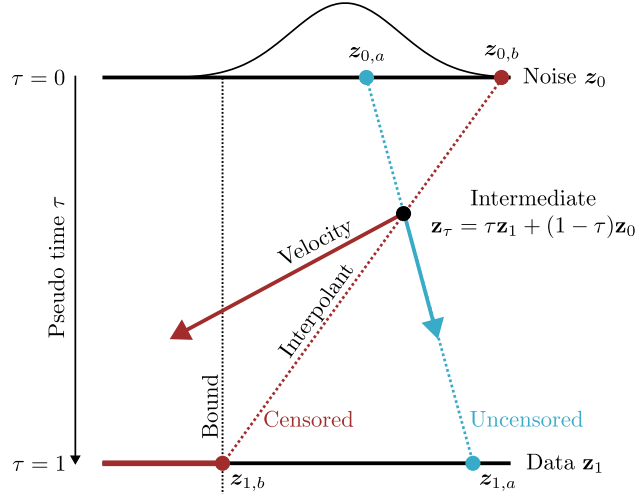


Fig. B5 Schematic showing the principle of censored flow matching. For two data cases (a and b), we draw independent noise during training and estimate a linear interpolant (dotted lines), connect the data and the noise. For a (blue), the data sample, $z_{1,a}$, is not on the bound (uncensored) and the targetted velocity points toward the data. For b (red), the data sample, $z_{1,b}$, is on the bound and, hence, censored; the true data value is unknown, it is only known that it lies between $-\infty$ and the bound as indicated by the red horizontal line. Here, the targetted velocity points towards an increase in the probability that the recovered data exceeds the bound.

In this framework, the variational Gaussian distribution, Equation (B18), defines the latent distribution **before** the terminal state has been censored,

$$q_{\theta}(\tilde{\mathbf{z}}_1 | \mathbf{z}_{\tau}) = \mathcal{N}\left(\hat{\boldsymbol{\mu}}_{\theta}, \frac{1}{2}\left((1-\tau) \cdot \mathbf{s}(\tau)\right)^2 \mathbf{I}\right). \quad (\text{B20})$$

To censor the terminal state, we have to define a thresholding function that depends on the physical lower x_k^L and upper bound x_k^U , here for the k -th variable. The terminal state for each of the k variables and each of the l grid points is independently censored by using its latent bounds $z_{k,l}^L = (x_k^L - x_{t,k,l})/\sigma_{\text{clim},k}$ and $z_{k,l}^U = (x_k^U - x_{t,k,l})/\sigma_{\text{clim},k}$, respectively. The thresholding function reads

$$f(\tilde{z}_{1,k,l}) = \begin{cases} z_{k,l}^L, & \text{if } \tilde{z}_{1,k,l} < z_{k,l}^L \\ z_{k,l}^U, & \text{if } \tilde{z}_{1,k,l} > z_{k,l}^U \\ \tilde{z}_{1,k,l}, & \text{otherwise.} \end{cases} \quad (\text{B21})$$

Given a Dirac delta distribution centred around this thresholding function, $p(z_{1,k,l} | \tilde{z}_{1,k,l}) = \delta(z_{1,k,l} - f(\tilde{z}_{1,k,l}))$, we define the probability density function (PDF)

of the censored Gaussian distribution,

$$q_{\boldsymbol{\theta}}(z_{1,k,l} | \mathbf{z}_{\tau}) = \begin{cases} \frac{1}{s_k} \varphi\left(\frac{z_{1,k,l} - \mu_{\boldsymbol{\theta},k,l}}{s_k}\right), & z_{k,l}^L < \tilde{z}_{1,k,l} < z_{k,l}^U \\ \Phi\left(\frac{z_{k,l}^L - \mu_{\boldsymbol{\theta},k,l}}{s_k}\right), & \text{if } \tilde{z}_{1,k,l} = z_{k,l}^L \\ \Phi\left(\frac{\mu_{\boldsymbol{\theta},k,l} - z_{k,l}^U}{s_k}\right), & \text{if } \tilde{z}_{1,k,l} = z_{k,l}^U \\ 0, & \text{otherwise,} \end{cases} \quad (\text{B22})$$

with $\varphi(\cdot)$ as the PDF and $\Phi(\cdot)$ as the cumulative density function of a Gaussian distribution with mean 0 and standard deviation 1. This PDF of a censored Gaussian distribution basically maps all the density that exceeds the bound to exactly the bound, while the density between the bounds remains as usual.

Using this variational distribution in the variational flow matching framework, we obtain as loss function for censored flow matching,

$$\begin{aligned} J(\mu_{\boldsymbol{\theta},k,l}, s_k, z_{1,k,l}, z_{k,l}^L, z_{k,l}^U) \\ = \mathbf{I}(z_{k,l}^L < \tilde{z}_{1,k,l} < z_{k,l}^U) \left[\frac{1}{2 \cdot (s_k)^2} (u_{k,l} - \hat{v}_{\boldsymbol{\theta},k,l})^2 + \log(s_k) \right] \\ - \mathbf{I}(\tilde{z}_{1,k,l} = z_{k,l}^L) \left[\log \Phi\left(\frac{u_{k,l} - \hat{v}_{\boldsymbol{\theta},k,l}}{s_k}\right) \right] \\ - \mathbf{I}(\tilde{z}_{1,k,l} = z_{k,l}^U) \left[\log \Phi\left(\frac{\hat{v}_{\boldsymbol{\theta},k,l} - u_{k,l}}{s_k}\right) \right], \end{aligned} \quad (\text{B23})$$

with

$$\mathcal{L}_{\text{GenSIM}}(\boldsymbol{\theta}, \mathbf{s}) = \mathbb{E}_{\tau, \mathbf{z}_0, \mathcal{D}} \left[\sum_{k=1}^{n_{\text{vars}}} \sum_{l=1}^{n_{\text{grid}}} J(\mu_{\boldsymbol{\theta},k,l}, s_k, z_{1,k,l}, z_{k,l}^L, z_{k,l}^U) \right], \quad (\text{B24})$$

and $\mathbf{I}(\cdot)$ is the indicator function. The predicted velocity is no longer only used to estimate the dynamics but also to estimate the probability that the bound is exceeded [34]; the neural network is trained in a mixed classification-regression setting, also called Tobit model [80]. In settings with physical bounds, the resulting estimator for the velocities is consistent and gives an unbiased estimate of the true but only partially observed velocities [81]. As schematically shown in Fig. B5, the loss function pushes the velocity towards a prediction that exceeds the bound, when the observed data is exactly on the bound, while the velocity in the uncensored case remains the same.

To use the censored estimate in the sampler, we have to reduce the distribution to a point estimate, accounting for the censoring. Here, we treat the neural network prediction as point estimate that specifies the median of the velocity. At each integration step, we project with the predicted velocity the intermediate state to the terminal state and apply thresholding when the projected state exceeds the bound,

$$\hat{\mathbf{z}}_{1|\tau} = \text{minimum} \left(\text{maximum}(\mathbf{z}_{\tau} + \tau \hat{\mathbf{v}}_{\boldsymbol{\theta}}, (\mathbf{x}^L - \mathbf{x}_t) / \boldsymbol{\sigma}_{\text{clim}}), (\mathbf{x}^U - \mathbf{x}_t) / \boldsymbol{\sigma}_{\text{clim}} \right) \quad (\text{B25})$$

with $\text{minimum}(\cdot, \cdot)$ and $\text{maximum}(\cdot, \cdot)$ as minimum and maximum function, respectively. By applying Equation (B12), we obtain the velocity from the potentially thresholded projected state,

$$\hat{\mathbf{v}}_{\theta} = \frac{\hat{\mathbf{z}}_{1|\tau} - \mathbf{z}_{\tau}}{1 - \tau}. \quad (\text{B26})$$

This median estimate of the *thresholded* velocity provides a simple yet efficient way to produce samples that can remain directly on the bounds without introducing additional randomness as needed in a Monte-Carlo sampling scheme.

In preliminary experiments, we found that censored flow matching boosts the prediction performance compared to conventional flow matching, confirming that incorporating prior physical knowledge can improve generative modelling. The variational flow matching thereby paves a general way to incorporate prior physical knowledge into flow matching.

Appendix C Neural network architectures

We employ two different neural networks architectures: for GenSIM, we use a transformer that works on subdomains, while we use a U-ViT architecture [34, 62] for the deterministic model to efficiently process the full Arctic domain at once. Both architectures are described in the following.

C.1 Transformer architecture

The velocity for the generative flow is approximated by a neural network, which is trained to work on subdomains of size 80×80 . Our curvilinear mesh is a structured mesh with 512×512 non-Cartesian cells, which are partially masked due to land. Accounting for these considerations, we built our neural network around a diffusion transformer architecture [40], inspired by design choices from large language models and from recent efficient diffusion models [82].

The neural network takes as main input 24 channels—consisting of the six state variables \mathbf{z}_{τ} , the six sea-ice state variables \mathbf{x}_t , and the twelve atmospheric forcing variables $\mathbf{F}_{t:t+12\text{h}}$ (four variables for two time steps and four channels for the degree day features). The transformer needs as additional input the mesh in Cartesian coordinates in a north polar stereographic projection, and the land mask (1 = ocean, 0 = land). The scalar input that is converted into an embedding is comprised of the pseudo time $\tau \in [0, 1]$, the resolution in kilometer, and three labels for the distribution augmentation [35, 47].

Instead of mesh-based cell values, the transformer processes flattened word-like tokens without any ordering. Furthermore, due to self attention, the transformer scales quadratically with the number of tokens. Hence, we have to project the raw input cells into aggregated tokens through tokenisation.

Prior to tokenisation, all values on land are set to 0 and the land mask is added as additional channel to achieve a constant bias-like feature across unmasked cells. The tokenisation is a learnable linear projection without bias, which combines 2×2 cells into a token, reducing the data from 80×80 cells to 1600 tokens. To counter-act the

data compression, the layers inflate the number of channels from 24 to 512. The mesh is pooled by the average in the 2×2 window, while the mask is maximum pooled.

The scalar inputs are converted into an embedding concurrently to the input tokenisation. The pseudo time, resolution, and labels are independently processed by combining random Fourier features (RFF)[83], which expand the number of features to 512, with a linear layer, a Sigmoid Linear Unit (SiLU) activation function [84], and another linear layer, keeping the number of feature at 512. At the end, each of the three branches is added together and activated with a SiLU to obtain the embedding.

The tokens are processed in a sequence of 8 transformer blocks, in which self-attention blocks are interleaved with small multi-layer perceptrons (MLP). Each of the self-attention blocks and MLPs is added to a short skip connection that directly links the input to the output of each block [85]. All self-attention blocks have the same structure:

- The input is normalised by root-mean-squared normalisation (RMSNorm) [86] where the dimension-wise scaling coefficient is a linear combination of the embedding [40].
- The normalised tokens are converted into a queries, keys, and values by a linear projection without bias, each containing 8 heads and 64 features per head and per token.
- The queries and keys are normalised by RMSNorm with a learnable scaling parameter along the feature dimension.
- The queries and keys are rotated by a two-dimensional rotary positional embedding (RoPE) [42, 87] based on the tokenised mesh and scaled by the resolution. This efficiently implement an anisotropic relative distance dependency into the self-attention block.
- After applying RoPE, multi-head self attention [41] is applied along the feature dimension, extracting 8 different spatial features per block.
- A linear projection without bias transforms the self-attention out back into 512 features per token.

Before added to the short-skipped tokens, the output of each self-attention block is multiplied by the tokenised mask to ensure that the land-masked tokens are always zero.

After adding the self-attention output to the tokens, an MLP is applied which has the following structure:

- Like for the self-attention block, the input to the MLP is normalised by RMSNorm and scaled dependent on the embedding.
- Afterwards, a linear layer without bias doubles the number of features per token to 1024.
- A gated SiLU activation function [88] activates the inflated features, before the output is deflated once again to 512 features by a linear projection without bias.

The output, multiplied by the mask, is added to the short-skipped tokens, like for the self-attention block.

To stabilise the transformer by imitating a U-Net-like architecture [89, 90], we implement long-skip connections, linking the output of the tokeniser to the input for the final head, linking the output of the first transformer block to the input of the last transformer block, and so forth. As linking function, we use a linear combination [82], which is dimension-wise modulated by the embedding.

In the end, also called the head, the tokens are normalised by RMSNorm and scaled with the embedding. To extract features that can contain sharp edges, we apply a rectified linear unit (ReLU) activation function after the normalisation. In the end, we linearly project the 512 features per token to 24 output features ($6 \cdot 2 \times 2$). Applying pixel shuffle [91], the output features are rearranged to form 6 predicted velocity values per cell.

The standard deviation \mathbf{s} , used in the censored flow matching model, is produced by a similar neural network to the embedding, combining RFFs with linear layers and a SiLU activation function. After adding the branches together and activating with a SiLU activation function, the output is linearly combined to 6 output features with a learnable bias term. To avoid negative standard deviations, we parametrise the output as its logarithm, $\log(\mathbf{s})$.

The transformer has in total 28.1×10^6 parameters, which is smaller than typical generative models for image generation [82] and for weather prediction [48]. In early experiments, we have seen that we could increase the number of layers and the feature dimensionality to around 500×10^6 parameters without overfitting to improve the scores. Yet, for efficiency, we constrain the number of parameters. The model for the standard deviation adds 1.6×10^6 parameters to the training of the generative flow.

C.2 U-ViT architecture

In addition to the transformer architecture for GenSIM, we use a U-ViT architecture for the deterministic model. This architecture combines U-Net like convolutional blocks [89] with a vision transformer [62] in its bottleneck. The convolutional blocks make it feasible to extract features on the pan-Arctic domain without subdomain decomposition. However, in contrast to self-attention, convolutional blocks are based on a fixed weighting, which assumes a local Cartesian mesh. We additionally have to modify the convolutions to handle the land mask [12, 34]. Throughout the U-ViT, prior to the application of convolutional layers and when skip connections are involved, the data is masked with the land mask, setting masked cells to zero: the convolutions are hence similar to partial convolutions without reweighting [92].

As for the transformer, the input data is masked, and the mask is added to the masked input data. A first convolutional layer (no bias, 1×1 kernel size) extracts 64 channels from the 18 inputted predictors ($6 \times$ sea-ice state, 4×2 atmospheric forcings, and $4 \times$ degree-day features). Concurrently, the neural network extract an embedding from the augmentation labels, as similarly done for the transformer.

Afterwards, 6 downsampling blocks reduce the spatial dimensions from 512×512 to 8×8 , while increasing the number of channels from 64 to 512. Each downsample block combines two ConvNeXt blocks [93] with a downsampling layer.

ConvNeXt blocks are inspired by transformer blocks: the initial convolutional layer (no bias, 7×7 kernel size) extracts spatial information, which is non-linearly combined by the subsequent multi-layer perceptron (MLP). The MLP has nearly the same structure as for the transformer with its RMSNorm modulated by the embedding. The output from the MLP is added to the block input in a short-skip connection.

The downsampling layer is a RMSNorm modulated by the embedding and followed by a convolutional layer (no bias, 2×2 kernel size, 2×2 stride size). While reducing the spatial dimension four times, the convolutional layer doubles the number of channels starting from the 64×64 resolution. The mask is concurrently coarse-grained by maximum pooling and a 2×2 window, keeping cell values if at least a single cell is unmasked in the window.

After reducing the resolution to 8×8 by the downsampling blocks, the bottleneck consists of 8 transformer blocks as they are similarly used in the transformer architecture: the extracted features and the reduced mask are flattened in space, while the mesh is averaged to the 8×8 resolution and flattened as well. The only difference between the transformer architecture and the bottleneck are the lower number of tokens in the bottleneck and its missing long skip connections.

The resolution of the features extracted by the bottleneck is increased by 6 upsampling blocks, which include long skip connections from the downsampling blocks to retain high-resolution features. The upsampling blocks mirror the strategy from the downsampling blocks with an upsampling layer followed by two ConvNeXt blocks.

The upsampling layer normalises the incoming features by RMSNorm, modulated by the embedding, before the resolution is doubled in x - and y -direction. To double the resolution, we use a convolutional layer (no bias, 1×1 kernel size) with pixel shuffle, as similarly used for the head in the transformer. Up to a resolution of 128×128 , the convolution halves the number of channels. The features with the increased resolution are combined with the features from the long-skip connection, outputted by the last ConvNeXt block from the downsampling block at the same resolution. As for the transformer, we linearly combine the features, where the channels-wise weighting stems from the embedding.

The head that uses the output from the last upsampling block works similar to the head of the transformer: a ReLU follows a normalisation with a modulated RMSNorm. As the head already works on the 512×512 resolution, the last layer only combines the extracted features with a convolution (1×1 kernel size) into predictions.

The convolutional layers add parameters to the neural network, while the bottleneck has the same number of parameters as the self-attention and MLP blocks from the transformer. In total, the U-ViT architecture has 32.2×10^6 parameters.